Draft version October 24, 2019
Typeset using LaTeX **twocolumn** style in AASTeX62

The Gas-Star Formation Cycle in Nearby Star-Forming Galaxies I. Assessment of Multi-scale Variations

Eva Schinnerer,[1,2] Annie Hughes,[3,4] Adam Leroy,[5] Brent Groves,[6,7] Guillermo A. Blanc,[8,9] Kathryn Kreckel,[1] Frank Bigiel,[10] Mélanie Chevance,[11] Daniel Dale,[12] Eric Emsellem,[13,14] Christopher Faesi,[1] Simon Glover,[15] Kathryn Grasha,[6] Jonathan Henshaw,[1] Alexander Hygate,[11] J. M. Diederik Kruijssen,[11] Sharon Meidt,[16] Jerome Pety,[17,18] Miguel Querejeta,[13,19] Erik Rosolowsky,[20] Toshiki Saito,[1] Andreas Schruba,[21] Jiayi Sun,[5] and Dyas Utomo[5]

[1] *Max Planck Institute for Astronomy, Königstuhl 17, 69117 Heidelberg, Germany*
[2] *Adjunct Scientist, National Radio Astronomy Observatory, 520 Edgemont Road, Charlottesville, VA 22903, U.S.A.*
[3] *Université de Toulouse, UPS-OMP, 31028 Toulouse, France*
[4] *CNRS, IRAP, Av. du Colonel Roche BP 44346, 31028 Toulouse cedex 4, France*
[5] *Department of Astronomy, The Ohio State University, 140 West 18th Ave, Columbus, OH 43210, USA*
[6] *Research School of Astronomy and Astrophysics, Australian National University, Canberra, ACT 2611, Australia*
[7] *International Centre for Radio Astronomy Research, The University of Western Australia, Crawley, WA 6009 Australia*
[8] *The Observatories of the Carnegie Institution for Science, 813 Santa Barbara Street, Pasadena, CA 91101, USA*
[9] *Departamento de Astronomía, Universidad de Chile, Casilla 36-D, Santiago, Chile*
[10] *Argelander-Institut für Astronomie, Universität Bonn, Auf dem Hügel 71, 53121 Bonn, Germany*
[11] *Astronomisches Rechen-Institut, Zentrum für Astronomie der Universität Heidelberg, Mönchhofstraße 12-14, 69120 Heidelberg, Germany*
[12] *Department of Physics and Astronomy, University of Wyoming, Laramie, WY 82071, USA*
[13] *European Southern Observatory, Karl-Schwarzschild-Strasse 2, D-85748 Garching bei München, Germany*
[14] *Univ. Lyon, Univ. Lyon1, ENS de Lyon, CNRS, Centre de Recherche Astrophysique de Lyon UMR5574, F-69230 Saint-Genis-Laval, France*
[15] *Institüt für Theoretische Astrophysik, Zentrum für Astronomie der Universität Heidelberg, Albert-Ueberle-Strasse 2, 69120 Heidelberg, Germany*
[16] *Sterrenkundig Observatorium, Universiteit Gent, Krijgslaan 281 S9, B-9000 Gent, Belgium*
[17] *IRAM, 300 rue de la Piscine, F-38406 Saint Martin de Hères, France*
[18] *Sorbonne Université, Observatoire de Paris, Université PSL, École normale supérieure, CNRS, LERMA, F-75005, Paris, France*
[19] *Observatorio Astronómico Nacional (IGN), C/Alfonso XII 3, Madrid E-28014, Spain*
[20] *4-183 CCIS, University of Alberta, Edmonton, Alberta, Canada*
[21] *Max-Planck-Institut für extraterrestrische Physik, Giessenbachstraße 1, D-85748 Garching, Germany*

ABSTRACT

The processes regulating star formation in galaxies are thought to act across a hierarchy of spatial scales. To connect extragalactic star formation relations from global and kpc-scale measurements to recent cloud-scale resolution studies, we have developed a simple, robust method that quantifies the scale dependence of the relative spatial distributions of molecular gas and recent star formation. In this paper, we apply this method to eight galaxies with $\sim 1''$ resolution molecular gas imaging from

the PHANGS-ALMA and PAWS surveys that have matched resolution, high quality narrowband Hα imaging. At a common scale of 140 pc, our massive ($\log(M_\star[M_\odot]) = 9.3 - 10.7$), normally star-forming ($SFR[M_\odot\,yr^{-1}] = 0.3 - 5.9$) galaxies exhibit a significant reservoir of quiescent molecular gas not associated with star formation as traced by Hα emission. Galactic structures act as backbones for both molecular and H II region distributions. As we degrade the spatial resolution, the quiescent molecular gas disappears, with the most rapid changes occurring for resolutions up to $\sim$0.5 kpc. As the resolution becomes poorer, the morphological features become indistinct for spatial scales larger than $\sim$ 1 kpc. The method is a promising tool to search for relationships between the quiescent or star-forming molecular reservoir and galaxy properties, but requires a larger sample size to identify robust correlations between the star-forming molecular gas fraction and global galaxy parameters.

Keywords: galaxies: ISM — ISM: atoms — ISM: molecules

1. INTRODUCTION

The star formation rate of galaxies reflects the interplay of galactic dynamics, violent stellar feedback (also from active galactic nuclei (AGN) if present), and gravitational collapse of molecular gas. Accessing these physics requires high resolution observations spanning large areas across a diverse sample of galaxies.

Observations at coarse resolution, from $\sim$ 1 kpc scales up to whole galaxies, show a tight correlation between molecular gas and star formation (e.g., Young et al. 1995; Kennicutt 1998b; Wong & Blitz 2002; Leroy et al. 2008; Bigiel et al. 2008; Schruba et al. 2011; Saintonge et al. 2011; Leroy et al. 2013; Momose et al. 2013, among many others). To the extent that galactic morphology remains discernible at these scales, such studies have typically found that maps of molecular gas and star formation tracers are very similar.

High resolution observations suggest a more complex picture. When the resolution approaches the scale of individual giant molecular clouds (GMCs) and HII regions, tracers of recent massive star formation and cold molecular gas appear spatially distinct (e.g., Kawamura et al. 2009; Schruba et al. 2010; Gratier et al. 2012; Battersby et al. 2017; Kreckel et al. 2018; Querejeta et al. 2019). This separation between the input (GMCs) and output (HII regions) of the star formation process has been interpreted as a sign of destructive feedback and used to estimate molecular cloud lifetimes (e.g., Kawamura et al. 2009; Schruba et al. 2010; Gratier et al. 2012; Kruijssen & Longmore 2014; Battersby et al. 2017; Kruijssen et al. 2018, 2019). A related measurement shows that the scatter in star formation–gas scaling relations increases with improving spatial resolution (e.g., Bigiel et al. 2008; Blanc et al. 2009; Schruba et al. 2010; Onodera et al. 2010; Leroy et al. 2013; Kreckel et al. 2018). This, too, has been interpreted as a signature of evolutionary cycling and/or feedback (e.g., Feldmann et al. 2011; Kruijssen & Longmore 2014; Kruijssen et al. 2018). Observations at high spatial resolution can potentially measure the impact of stellar feedback on the gas and thus lead to a better understanding of the mechanisms that determine the efficiency of star formation.

High resolution observations also reveal the importance of galactic dynamics. The organization of star formation by dynamically induced gas flows and dynamical suppression of star formation becomes evident when observations reach scales smaller than the characteristic sizes/widths of dynamical features like bars and spiral arms. As a result, high resolution observations offer insight into how galaxy morphology affects where stars are born. For example, at high resolution, star-forming regions tend to appear downstream of the arms seen in gas (e.g., see Schinnerer et al. 2013; Egusa et al. 2017; Schinnerer et al. 2017; Kreckel et al. 2018). Studying M51, Meidt et al. (2013) and Schinnerer et al. (2013) identified strong variations in the ratio between the star formation rate and the molecular gas mass (see also Leroy et al. 2017a). Most strikingly, they found regions in the inner spiral arms that have immense gas reservoirs but little star formation. Meidt et al. (2013) attributed these features to dynamical suppression of star formation (which also manifests in early type galaxies at larger scales, e.g., Davis et al. 2014) rather than the absence of high density gas (as confirmed by Querejeta et al. 2019).

To date, most high resolution work has focused on case studies of individual galaxies. Studies targeting samples of many galaxies have achieved at best a few hundred pc to ~kpc resolution, and often treated whole galaxies as a single unit. A clear next step is to systematically examine how tracers of massive star formation compare to tracers of molecular gas at high resolution across a large sample.

In this paper, we compare CO emission, tracing molecular gas, to Hα emission, tracing recent star formation, across a large area in eight nearby galaxies. Our maps all have spatial resolution of 140 pc, and often better. This means that an individual resolution element approaches the size of a large GMC or HII region and that we expect

only one or a few such regions per beam. Our sample shows diverse morphologies, including spiral arms, bars, nuclear starburst rings, and flocculent structure. This allows a comparative analysis and offers the chance to identify general and environmental trends, which was challenging with previous individual-galaxy case studies.

Specifically, we compare the location of Hα emission, a classic tracer of recent massive star formation (e.g., reviews by Kennicutt 1998b; Kennicutt & Evans 2012) to the location of CO emission, a tracer of molecular gas (e.g., reviews by Fukui, & Kawamura 2010; Bolatto et al. 2013; Heyer, & Dame 2015). We divide each galaxy into regions where only CO emission is bright, only Hα emission is bright, or both tracers are bright. Then, we quantify the fraction of lines of sight and the fraction of emission from each type of region. We repeat this analysis for each galaxy for a range of spatial resolutions. We examine the changing statistics and morphology of the two tracers as a function of scale. Doing so, we quantify how the coincidence of gas and star formation observed at low resolution changes as we resolve galaxies at the scale of an individual star-forming region.

The PHANGS (Physics at High Angular resolution in Nearby GalaxieS[1]) collaboration is carrying out high physical resolution surveys of molecular gas and star formation tracers in many nearby galaxies. The observations enabling this analysis are $\sim 1''$ resolution CO line emission maps from the PHANGS-ALMA survey (Leroy et al. in prep.), which is mapping CO emission from the disks of ∼80 nearby galaxies with high fidelity for the first time. This angular resolution matches that of seeing-limited Hα observations and allows $\lesssim 100$ pc resolution out to distances of up to ~ 18 Mpc. For comparison, previous large CO surveys typically achieved $\sim 10 - 45''$ resolution or targeted only the innermost parts of galaxies with limited sensitivity.

The paper is organized as follows: The data used are presented in §2. We describe our methodology in §3, present our results in §4, and discuss the implications of our findings in §5. We summarize our findings in §6.

2. DATA

We require high spatial resolution imaging of the molecular gas and a tracer of recent star formation on scales of $\lesssim$100 pc. This ensures that each individual resolution element approaches the size of a giant molecular cloud (Sanders et al. 1985) or a massive H II region (Oey et al. 2003; Azimlu et al. 2011).

To trace recent massive star formation, we use narrow-band Hα+[N II] imaging. At the $d < 17$ Mpc distance to our targets, seeing-limited images achieve $\approx 1'' \lesssim$ 100 pc resolution. We pair these with $\approx 1''$ resolution low-J CO line imaging to trace the molecular gas.

We analyze the first seven galaxies targeted by PHANGS-ALMA (Leroy et al. in prep.), which also have Hα imaging of sufficient quality for our analysis. Our sample also includes the grand-design spiral galaxy M 51 using data from the PAWS survey (Schinnerer et al. 2013). We summarize the final sample of eight galaxies in Table 1.

[1] www.phangs.org

Table 1. Key Parameters of Sample Galaxies.

Name	Distance (Mpc)	Inclination (degrees)	R_{25} (arcmin)	SFR ($M_\odot$ yr^{-1})	log($M_\star$) ($M_\odot$)	$A_{V,MW}$ (mag)	Metallicity log($\frac{O}{H}$)$_{PP04}$	Hubble Type	Activity
NGC 0628	9.8	9	4.9	1.83	10.2	0.192	8.51	Sc-A	HII
NGC 3351	10.0	45	3.6	1.30	10.2	0.076	8.80	Sb-B	HII; Sbrst
NGC 3627	10.6	55	5.1	3.54	10.6	0.091	8.74	Sb-AB	LINER; Sy 2
NGC 4254	16.8	38	2.5	5.44	10.5	0.106	8.68	Sc-A	LINER; HII
NGC 4321	15.2	38	3.0	3.81	10.6	0.072	8.71	Sbc-AB	LINER; HII
NGC 4535	15.8	41	4.1	2.22	10.4	0.053	8.78	SAB(s)c	LINER; HII
NGC 5068	5.2	27	3.7	0.29	9.3	0.281	8.35	Scd-AB	–
NGC 5194	8.6	21	6.9	4.91	10.7	0.096	8.70	SA(s)bc pec	HII; Sy2.5

NOTE—The galaxy parameters are adopted from Leroy et al. (2019) where the original references can be found. For NGC 4535, the Hubble type and activity are taken from NED.

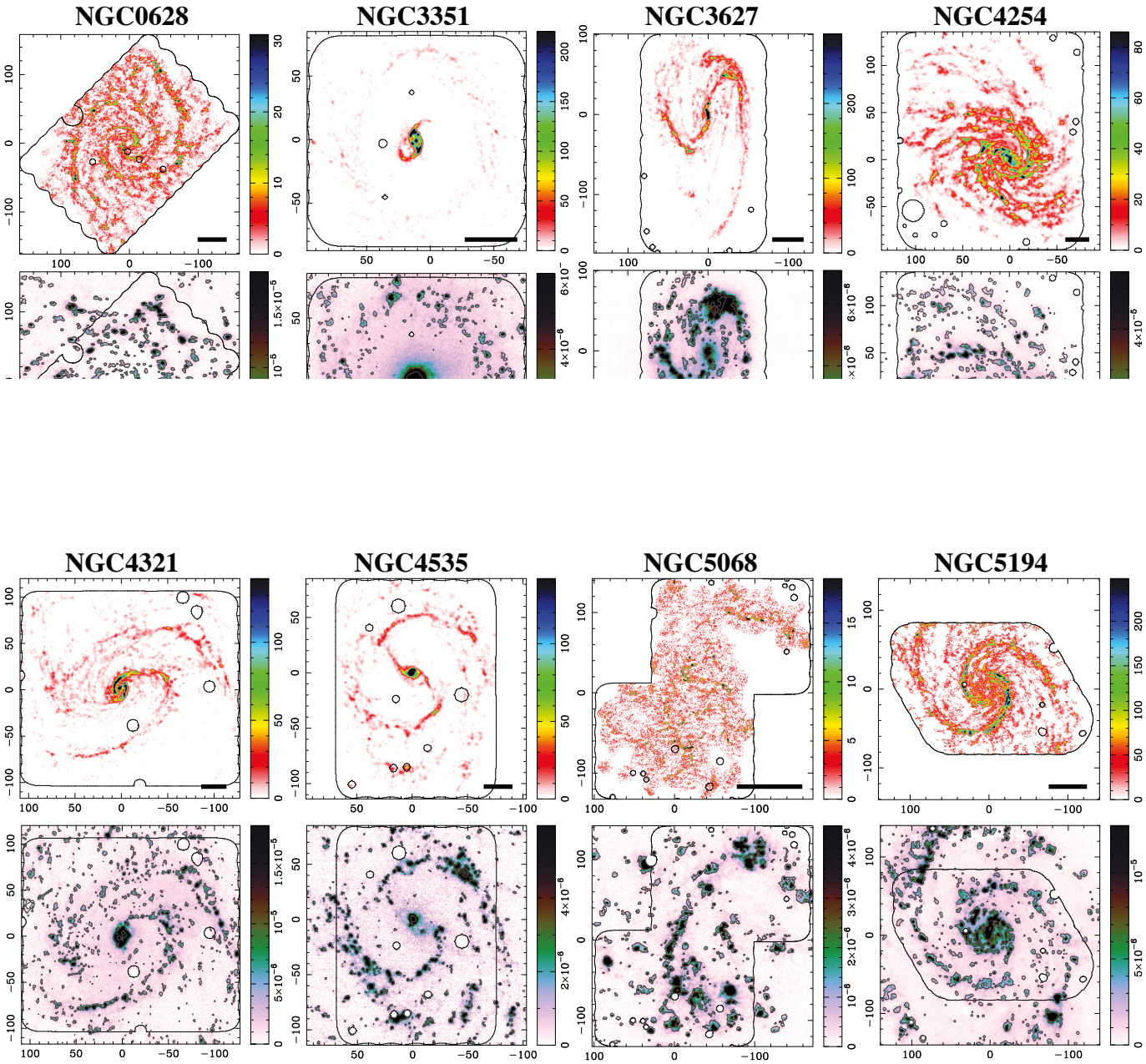

Figure 1. Gallery of CO integrated intensity (*first and third row*) and Hα maps (*second and fourth row*) used in this paper. The galaxies shown (*from left to right*) are NGC 0628, NGC 3351, NGC 3627 and NGC 4254 (*top two rows*), and NGC 4321, NGC 4535, NGC 5068 and NGC 5194 (*bottom two rows*). The outer black contour in the CO (Hα) maps indicates the edge of our analysis region, i.e., the field that is common to both the CO and Hα datasets. Empty circles indicate masked foreground stars or background galaxies. Note that we use a linear color stretch that is different for each galaxy, and for which saturation corresponds to the $10^{\rm th}$ percentile value in each map. The CO maps are displayed in units of $\mathrm{K\,km\,s^{-1}}$. The Hα maps, which are corrected for [N II] contribution $f_{\rm NII}$, Hα transmission $T_{\rm H\alpha}$ and foreground Galactic extinction $\mathrm{A_{V,MW}}$, are in units of $\mathrm{M_\odot\,yr^{-1}}$. The emission that we identify with H II regions is indicated with a gray contour on the Hα maps (see Section 2.2.5). The axes are in offset arcseconds from the reference position of each map. The black bar in the bottom right corner of each CO intensity map indicates a spatial scale of 2 kpc.

Table 2. Datasets and Parameters used for CO and Hα maps.

Name	FoV_{CO}	σ_{CO}	θ_{CO}	$\theta_{best,CO}$	L_{CO}	f_{CO}	$\theta_{H\alpha}$	$\theta_{best,H\alpha}$	f_{NII}	$T_{H\alpha}$	$L_{H\alpha,int}$	SFR	f_{DIG}	$\log L_{H\alpha,min}$
	("×")	($K\,km\,s^{-1}$)	(")	(pc)	($10^8\,K\,km\,s^{-1}\,pc^2$)		(")	(pc)			($10^{41}\,erg\,s^{-1}$)	($M_\odot\,yr^{-1}$)		$erg\,s^{-1}$
(1)	(2)	(3)	(4)	(5)	(6)	(7)	(8)	(9)	(10)	(11)	(12)	(13)	(14)	(15)
NGC0628	319×319[a]	0.8	1.12	60	1.85	0.72	1.73	**90**	0.019	0.938	0.7	0.4	0.39	37.5
NGC3351	172×166[a]	0.7	1.46	**80**	0.92	0.65	1.16	60	0.209	0.972	0.6	0.3	0.56	36.8
NGC3627	158×273[a]	0.9	1.57	**90**	6.14	0.91	1.44	80	0.223	0.986	1.6	0.9	0.41	36.8
NGC4254	199×232[a]	0.4	1.71	**140**	11.88	0.86	1.52	130	0.235	0.979	4.8	2.6	0.40	36.8
NGC4321	237×211[a]	0.5	1.64	**130**	5.67	0.76	1.28	100	0.112	0.838	1.6	0.9	0.58	36.5
NGC4535	145×199[a]	0.5	1.56	**120**	2.89	0.72	1.23	100	0.168	0.915	0.8	0.4	0.49	36.8
NGC5068	269×274[a]	1.3	1.00	30	0.06	0.31	1.34	**40**	0.0770	0.993	0.3	0.2	0.35	37.3
NGC5194	280×180[b]	4.4	1.06	50	10.97	0.95	1.83	**80**	0.228	0.983	1.4	0.7	0.47	37.3

[a] $^{12}CO(J = 2 \rightarrow 1)$ observed by ALMA, Leroy et al. (in prep.)

[b] $^{12}CO(J = 1 \rightarrow 0)$ observed by IRAM, Schinnerer et al. (2013); Pety et al. (2013)

[c] CTIO 1.5m, 14.5'×14.5' FoV, CT6586/20 filter, SINGS 5th delivery document[2]

[d] KPNO 2.1m, 10.2'×10.2' FoV, KP1563 filter, SINGS 5th delivery document

[e] KPNO 2.1m, 10.2'×10.2' FoV, KP1564 filter, SINGS 5th delivery document

[f] MPG 2.2m/WFI, 16'×16', 856 filter, Razza et al. (in prep.)

[g] CTIO 1.5m, 10.2'×14.3' FoV, MCELS6568/30 filter, Meurer et al. (2006)

NOTE—Summary of data products used for the CO and Hα emission as well as relevant parameters derived for each data product. The information provided for column: (1) galaxy name, (2) size of the area mapped in CO line emission, (3) characteristic 1σ sensitivity corresponds to the average RMS across the integrated intensity CO map at the resolution given in column (4), (4) angular resolution refers to the round Gaussian CLEAN beam used for restoration; except for NGC 5194 where the geometric mean of the elliptical CLEAN beam is given, (5) highest native spatial resolution achieved in CO (If the resolution of the CO data sets the limiting spatial scale of our analysis, it is highlighted in bold-face.), (6) integrated CO line flux present in the final maps used for our analysis (i.e. after applying a threshold at $12.6\,M_\odot\,pc^{-2}$ at 140 pc resolution and artifact mask, within the common FoV), (7) fraction of integrated CO emission contained in maps used for the analysis (see column (6)) relative to integrated CO emission in the PHANGS-ALMA internal data release v3.3 cube[3], (8) angular resolution of the Hα maps ($\theta_{H\alpha}$) as determined on stars in the maps, (9) highest native spatial resolution achieved in Hα (If the resolution of the Hα data sets the limiting spatial scale of our analysis, it is highlighted in bold-face.), (10) NII fraction f_{NII} as determined taking the filter response curves into account (see text for details), (11) transmission correction for Hα $T_{H\alpha}$ as determined taking the filter response curves into account (see text for details), (12) integrated Hα line emission present in the final maps used for our analysis (i.e. within our FoV and with foreground stars masked). (13) SFR based on integrated Hα line emission (from column (13)) present in map used for analysis, (14) contribution of DIG emission to total Hα emission, and (15) minimum HII region luminosity, calculated as the Hα surface brightness threshold integrated over the beam area, corresponding to our DIG separation strategy.

2.1. *CO Images*

PHANGS-ALMA imaged the CO(2-1) emission in our targets using the ALMA 12-m, 7-m, and total power antennas. In this paper, we use a pilot sample observed during Cycle 1 (project 2012.1.00650.S; NGC 0628) and Cycle 3 (projects 2013.1.00925.S and 2013.1.00956.S; remaining galaxies except NGC 5194). We chose our target area to match the region of active star formation indicated by an intensity contour of $1\,\mathrm{MJy\,sr^{-1}}$ in the WISE 22 micron image.

We use integrated intensity maps constructed from the data cubes delivered in PHANGS-ALMA internal data release 3.3 as our starting point. The construction of these maps is described in Leroy et al. (in prep.), and their properties are summarized in Tab. 2. Briefly, these were imaged in CASA 5.4.0. They should be sensitive to emission on all spatial scales due to the inclusion of data from both the 12-m array and the Morita Atacama Compact Array (ACA). Four of the galaxies (NGC 3627, NGC 4254, NGC 4321, and NGC 5068) were observed in two separate large (100+ pointings) mosaics. We match the beams of the two halves via convolution and combined them via linear mosaicking. This results in moderately different noise properties for the two halves of the map. After calibration and imaging, the resulting data cubes were convolved to have a round beam. The typical RMS noise in brightness temperature units is $\sigma_{RMS} \approx 0.17\,\mathrm{K}$ per $2.5\,\mathrm{km\,s^{-1}}$ channel, but varies slightly between cubes.

We use the integrated intensity maps delivered in the internal data release v3.3. These are constructed by applying a "broad" signal identification mask to the spectral line cube before summing all valid pixels across the observed velocity range. Specifically, the broad mask is the logical union of two signal identification masks, the first generated from the data cube at the best available resolution and the second from a version of the cube that has been smoothed to a spatial resolution of 500 pc. In both cases, we identify emission above 3.5σ in 3 consecutive channels of the cube, and expand it to include contiguous regions in (x, y, v) space that show emission above 2σ over 2 consecutive channels. The resulting "broad" integrated intensity maps have high completeness, meaning that they include most CO emission in the cube, even emission present at only modest signal-to-noise. More quantitatively, the flux recovery in the v3.3 broad integrated intensity maps (which are our input maps for the analysis) varies between 93% (NGC 4321) and 99% (NGC 3627) of the total CO flux that is present in the input best resolution data cube (see also discussion in Sun et al. 2018). Sensitivity estimates for these integrated intensity maps are tabulated in Tab. 2. These are spatial averages of the sensitivity across each map, calculated as $\sigma_{\mathrm{RMS}} \times \sqrt{N} \times \Delta v$, where N is the number of channels in the signal identification mask for that sightline, and Δv is the channel width. The equivalent inclination-corrected 1σ integrated molecular mass surface density sensitivity limits vary between 2.5 and $7.4\,\mathrm{M_\odot\,pc^{-2}}$ across the PHANGS galaxies, assuming a standard Galactic conversion factor of $\alpha_{\mathrm{CO}} = 4.35\,\mathrm{M_\odot\,pc^{-2}\,(K\,km\,s^{-1})^{-1}}$ (Bolatto et al. 2013) and a $^{12}\mathrm{CO}(J = 2 \rightarrow 1)$ to $^{12}\mathrm{CO}(J = 1 \rightarrow 0)$ brightness temperature ratio of $R_{21} = 0.7$.

For NGC 5194 (M51), we use the $1''$ resolution integrated CO(1-0) image from PAWS (PdBI Arcsecond Whirlpool Survey, Schinnerer et al. 2013). PAWS combined observations from the IRAM PdB interferometer and 30m single dish telescope, ensuring that the map includes emission on all spatial scales (see Pety et al. 2013). Details of the observations and data reduction are presented in Pety et al. (2013). The PAWS map has an average 1σ sensitivity of $\sim 4.4\,\mathrm{K\,km\,s^{-1}}$, corresponding to an integrated mass surface density sensitivity of $\sim 19\,\mathrm{M_\odot\,pc^{-2}}$.

2.2. *Hα Images*

We use narrowband Hα imaging to trace recent massive star formation, drawing from a mixture of new and literature data. For the literature data, we adopt the image that best matched the following criteria: (i) field-of-view (FoV) sufficient to cover the CO data, (ii) angular resolution similar to the CO data, and (iii) a corresponding R band image observed with the same telescope under similar conditions. For several galaxies where no literature data matched our criteria, we obtained new Wide-Field Imager (WFI) narrowband and R band imaging using the MPG/ESO 2.2m telescope. Details on the datasets used can be found in Tab. 2.

Specifically, we used data from the SINGS ancillary survey (Kennicutt et al. 2003) for NGC 0628, NGC 3351, NGC 4254, NGC 4321, and NGC 5194. Details of the observations, including the associated R band data used for continuum subtraction, can be found in the SINGS fifth delivery document[4]. The continuum R band data reach a depth of 25 mag/arcsec^2 with a signal-to-noise of $\sim$10. The Hα narrowband filter data were observed for 1800 s.

NGC 5068 was observed in the Hα narrowband and R band as part of the Survey for Ionization in Neutral Gas Galaxies (SINGG; Meurer et al. 2006) at the CTIO.

[4] http://irsa.ipac.caltech.edu/data/SPITZER/SINGS/doc/sings_fifth_delivery_v2.pdf

NGC 5068 was also observed for 1800 s in the narrowband, and 360 s in the R band.

For NGC 3627 and NGC 4535, the literature data were not of sufficient quality to match our criteria. Therefore, we use data from a new survey of PHANGS targets using the WFI instrument on the MPG/ESO 2.2-m telescope at La Silla Observatory. This survey obtained both narrowband Hα and Rc band using WFI. The galaxies were placed in a single CCD, avoiding chip gaps, allowing an uninterrupted FoV of 16'×16'. These data were astrometrically and photometrically calibrated using GAIA DR2 catalogs cross-matched to all stars in the full FoV of the WFI images. Full details of this survey, including observations, reduction, calibration and sky subtraction can be found in Razza et al. (in prep.).

2.2.1. *Sky subtraction*

We subtract a sky background from the SINGS Hα data. To do this, we first mask all bad pixels and bright sources. Then, we mask all emission that exceeds the median of the remaining image by > 3 times the rms noise. We convolve this mask by $\sim 3 \times$ FWHM to further mask out any diffuse light from bright sources or the galaxy. We then fit and subtract a plane from the masked image. In all cases, our targets fill a significant fraction of the image. In a few cases this caused the plane fit to fail. In these cases, the sky background was set to be the median of the masked image. The typical sky brightness was 20-21 mag/arcsec^2 in the R band images.

For NGC 5068 and our WFI data, the images are already sky subtracted by Meurer et al. (2006) and Razza et al. (in prep.), respectively. We repeated the above analysis and confirm that the residuals appear consistent with noise.

2.2.2. *Seeing and astrometry*

After sky subtraction, we fit all point sources in both the Hα and R band images to determine the average seeing[5]. When the seeing differed significantly between the R band and Hα images (> 0.5 pixel), we convolved the higher resolution data to match the lower resolution. Typical seeing for the data range from 1.″2 to 2.″1 (see Tab. 2 for individual galaxies).

For the SINGS and SINGG data, the astrometry was already confirmed by matching stellar sources to the US Naval Observatory A2.0 database (Monet 1998). Meurer et al. (2006) matched ~ 100 and found an accuracy of 0.″4, similar to the 0.″5 found for the SINGS data.

[5] This was done using the IDL implementation of the DAOPHOT routines `APER` and `GETPSF`: https://idlastro.gsfc.nasa.gov/ftp/pro/idlphot/aper.pro.

We require accurate absolute astrometry to assess spatial offsets between Hα and CO emission. Therefore, we used Gaia DR2 (Gaia Collaboration et al. 2016, 2018) to further refine the absolute astrometry. We fit ~ 50 stars per R band image with an rms of $\sim$50–60 mas on the required offsets which we applied. This yielded a final astrometric accuracy of 0.″1–0.″2. The astrometry of the WFI images was calculated using the Gaia DR2 catalog directly and so already reach this same level of accuracy.

2.2.3. *Continuum subtraction*

Once the Hα and R band images are aligned and at the same resolution, we determine the scale of the R band continuum in the Hα narrowband image. If the images are correctly flux calibrated, this scale should be one. However to confirm this we determine the median flux ratio of the matched non-saturated stars between the narrowband and R band images.

Using this flux ratio as a basis, we obtain a first estimate of the Hα flux by subtracting the R band image from the narrowband. However, the Hα+NII line also contributes to the R band data. Therefore, using the estimated Hα+NII image we determine the Hα+NII contribution to the R band image. We subtract this estimated line contamination from the R band image and iterate this process until successive continuum estimates differ by less than 1%. Then we subtract this continuum estimate to achieve a flux-calibrated line image.

Note that this approach does not account for a varying continuum slope in the R band. We might expect some variation in the narrowband continuum to R band continuum ratio due to, e.g., a variation in the stellar population across the galaxy disk (Razza et al. in prep.).

2.2.4. *Correction for transmission, [NII] contamination, and Galactic extinction*

We correct for transmission loss of the Hα emission line, which can be red-shifted out of the chosen narrowband filter, and for the contribution of the [N II]λ6548, 6583 emission lines, which may fall within the narrowband filters.

To do this, we use an integrated, high signal-to-noise HII region spectrum from the MUSE observations of NGC 0628 presented in Kreckel et al. (2016). We treat this as a characteristic spectrum for all of our targets. Our targets are all relatively massive, relatively face-on spiral galaxies, so we expect the NGC 0628 spectrum to be reasonably representative of the typical HII region in our sample. The NGC 0628 template spectrum has an intrinsic [NII]/Hα ratio of 0.3. This is close to, but slightly lower than some of the global estimates for the [NII]/Hα in our targets from, e.g., Kennicutt et al.

(2011). We note possible variation in [NII]/Hα as a source of uncertainty.

We shift this template spectrum to the redshift of each galaxy. Then, using the transmission curves for the filters listed in the notes of Tab. 2, we calculate the contribution of the Hα and [NII] lines to the narrowband image (see Tab. 2). Based on this calculation, we subtract the likely contamination by [NII] to create an Hα-only surface brightness image ($F_{\mathrm{H}\alpha} = F_{\mathrm{line}}(1 - f_{[\mathrm{NII}]})/T_{\mathrm{H}\alpha}$).

As a final step, we correct all images for foreground Galactic extinction using the map of Schlafly & Finkbeiner (2011).

2.2.5. *Filtering out emission from diffuse ionized gas (DIG)*

Our analysis uses Hα emission to pinpoint the spatial location of recent high-mass star formation, i.e., we are specifically interested in Hα emission arising from HII regions that surround massive stars. In this context, Hα emission arising from diffuse ionized gas (DIG) must be excluded from the analysis. This Hα emission does not originate from gas that is ionized locally by young massive stars. Unfortunately, DIG can contribute 50% or more to the observed Hα flux of a galaxy (e.g., review by Haffner et al. 2009). The origin of the ionizing photons producing the DIG is still debated, with some or indeed all of these photons originating from massive young stars (e.g., due to Lyman-continuum leakage from H II regions; Weilbacher et al. 2018). For our purposes, the key issue is that the DIG emission is not necessarily co-spatial with the young stellar population powering the HII regions (see, e.g., Kreckel et al. 2016). Instead DIG generally exhibits a more smooth appearance.

There are two main methods to separate the Hα emission arising from HII regions and the gas associated with the DIG. The first method, based on morphology, decomposes the Hα maps into bright knots and a diffuse background (e.g., Thilker et al. 2002; Oey et al. 2007) using for example the software HIIPHOT (Thilker et al. 2000). Alternatively, optical spectroscopy can be used to identify emission arising from DIG, which is warmer and less dense than the HII region gas (e.g. Blanc et al. 2009; Haffner et al. 2009; Kaplan et al. 2016; Tomičić et al. 2017).

After correcting for Galactic extinction, we attempt to remove the DIG contribution from our Hα maps. We use the following unsharp masking scheme which is qualitatively similar to the approaches mentioned above. We implemented a two step approach which is first identifying diffuse emission on scales larger than HII regions, and in a second iteration attempting to take into account variations in the strength of the DIG contribution on the scales of galactic structures such as spiral arms. The filtering scales and gain represent tuning parameters informed by physical expectations:

1. **Unsharp mask with a 300 pc kernel:** We smooth our original image with a Gaussian kernel with FWHM 300 pc. We choose 300 pc because we do not expect HII regions to reach sizes much larger than that scale (e.g., Oey et al. 2003; Azimlu et al. 2011; Whitmore et al. 2011). Then, we subtract this smooth version of the image from the original image. We identify likely HII regions as the parts of the map still detected at high signal-to-noise in this filtered map.

2. **Subtract a scaled version of the initial HII regions from the DIG map:** We subtract a scaled version of the HII regions identified in the previous step from the original map. The scaling factor, which is 0.33, reflects that this is an initial estimate and that we do not want to oversubtract at this stage.

3. **Unsharp mask with an 750 pc kernel:** We smooth our HII region subtracted image with a Gaussian kernel that has FWHM 750 pc. This scale is large enough to typically encompass galactic structures, such as spiral arms, that might show higher levels of DIG contribution and clustering of HII regions (e.g. Kreckel et al. 2016). Then, we subtract this smooth version of the image from the *original* image. We identify our final set of HII regions as the parts of the map still detected at high signal-to-noise in this filtered map.

We proceed by blanking all regions outside the identified HII regions and treating the masked map as our best estimate for the location of massive star formation. The final Hα maps used for our analysis are constructed by applying this mask to the calibrated and corrected Hα map. The flux in this masked map represents our best estimate of the relative intensity of star formation, because we expect most of this Hα emission to arise from gas photo-ionized by massive stars (rather than, e.g., shocks). On average, this process removes $\sim 50\%$ of the Hα emission from the initial maps.

The tuning parameters that we adopted were optimized to yield a procedure that identifies bright knots of Hα emission, which are likely HII regions, when applied to our whole sample. Three of the authors independently inspected the resulting masks to confirm that they indeed isolate the bright knots in each of our Hα maps, without subdividing the emission from large HII regions. In a few targets, we further confirmed that our approach agrees sufficiently well with masks based

on HIIPHOT and with spectroscopic separation of DIG and HII regions (Kreckel et al. 2016; Blanc et al. 2009). We experimented with fixed surface brightness cuts to separate the Hα emission into the DIG and the H II regions, but found the resulting masks to be much less satisfactory. This is likely linked to the fact that the Hα luminosity of HII regions depends on the exact physical conditions present in the ionized gas such as ionizing flux, gas geometry etc. which can vary significantly between and within galaxies at our resolution. Lastly, we note that the vertical extent of the DIG can be significant reaching typical scale heights of 1 kpc (e.g. Rossa, & Dettmar 2003; Levy et al. 2019).

We note one important additional caveat about our strategy for DIG removal. When identifying bright regions during the unsharp masking steps, we use a signal-to-noise threshold. Because the noise and native resolution of the input Hα data vary, the effective Hα surface brightness threshold applied to our fiducial maps ranges from $I_{\mathrm{H}\alpha}[\mathrm{erg\,s^{-1}\,cm^{-2}\,sr^{-1}}] = 2.21 \times 10^{-6}$ (NGC 4254) to 9.46×10^{-6} (NGC 5068), corresponding to SFR surface density limits between 0.0014 and $0.0036\,\mathrm{M_\odot\,yr^{-1}\,kpc^{-2}}$. For a point source at the native resolution of our data, these sensitivity limits correspond to H II region luminosities between $\log_{10} L_{\mathrm{H}\alpha}[\mathrm{erg\,s^{-1}}] = 36.5$ (NGC 4321) and 37.6 (NGC 5194). These limits are comparable to the peak of the H II region luminosity function measured by narrowband Hα imaging in the literature (e.g. Bradley et al. 2006; Oey et al. 2007), although the current generation of optical IFUs are able to detect H II regions with lower luminosities (e.g. Kreckel et al. 2016; Rousseau-Nepton et al. 2018).

2.2.6. *No correction for internal extinction*

Our final Hα line flux images trace emission from H II regions without any correction for attenuation. We expect our images to do a good job tracing the location of massive star formation, but the maps may miss the most heavily extinguished regions. Because our analysis focuses mostly on the location (rather than the amount) of recent massive star formation, we expect this to be a secondary concern. Based on literature work in M 51 (Scoville et al. 2001; Schinnerer et al. 2017), we do not expect that such highly extinguished regions occupy a significant fraction of sightlines in the disks of our galaxies. For our analysis based on flux, the underestimation of flux is likely stronger for the regions co-located with molecular gas, where dust is likely well-mixed with the gas, than for regions where no gas is present.

3. METHODOLOGY

We aim to quantify the coincidence of molecular gas, traced by CO, and high-mass star formation, traced by Hα, across a range of spatial scales. To do this, we adopt the following approach:

1. **Threshold the Hα images:** The **removal of the significant** DIG contribution to the Hα images acts as a natural threshold (see § 2.2.5). We calculate the total flux in the thresholded image at this stage.

2. **Threshold the CO images:** We clip the CO images at our best matching resolution of 140 pc using a physical threshold of $12.6\,\mathrm{M_\odot\,pc^{-2}}$ (accounting for galaxy inclination) or roughly an $\mathrm{A_V} \approx 1$. This corresponds to the equivalent $3\,\sigma$ mass surface density sensitivity of our CO map with the lowest sensitivity at this spatial scale (NGC 5194).

3. **Convolve to coarser physical resolutions:** We convolve each thresholded image to a succession of coarser resolutions, ranging from our best matching resolution of 140 pc to 1.5 kpc (to match to previous studies working at coarser resolution).

4. **Clip the low intensity emission in the convolved images:** For each convolved image, we blank the faintest lines of sight that collectively contribute 2% of the total flux in the image. This suppresses convolution artifacts.

5. **Measure the coincidence of the two tracers at each resolution:** We divide each galaxy at each resolution into regions with visible CO only, visible Hα only, or both CO and Hα emission present. We measure the fraction of sightlines and the fraction of flux in each region type at each resolution.

This approach represents a specific application of a more general methodology, which would be to measure the joint distribution functions of CO and Hα. In the rest of this section, we motivate the specific choices that we have made. When describing the results in the next sections, we use the words 'sightlines' and 'pixels' interchangeably.

3.1. *Thresholding and total flux estimation*

We threshold both the CO and Hα images before comparing them. This fixes the total flux used in the analysis across scale. It also ensures that we have high confidence that all emission entering the analysis corresponds to real high-mass star formation or massive concentrations of molecular gas.

The total CO and Hα fluxes after thresholding within the common FoV of our 140 pc resolution images are

tabulated in Tab. 2. For Hα, our threshold is set by our DIG removal strategy (see § 2.2.5). For CO, we impose a mass surface density threshold that allows us to work exclusively with securely detected pixels across all our CO maps. For the CO emission, we do not impose any filtering analogous to what we used to subtract the DIG (from the Hα maps). Our reasoning is that while "diffuse" CO emission has been identified in galaxies (e.g., Pety et al. 2013; Caldú-Primo et al. 2015; Roman-Duval et al. 2016), the physical nature of this gas remains unclear. Extended CO emission still does indicate the presence of molecular gas, which may very well be in marginally bound clouds and available for star formation. This is not symmetric to the DIG, which represents emission not associated with local massive star formation. This is an important topic for future exploration, but in the interests of maintaining a simple, physically-motivated, and reproducible approach, we do not filter the CO emission.

For reference, our adopted CO threshold is roughly equivalent to a cut of $A_V \approx 1$ mag (e.g., Bohlin et al. 1978). This is close to the limit of $A_V = 2$ mag used by Heiderman et al. (2010) to define the boundaries of local molecular clouds in highly resolved maps. That is, our CO threshold already identifies only pixels where the emission averaged over a 140 pc beam matches that seen within highly resolved local GMCs.

Typically, this threshold retains about 75% of the total flux in the input CO data cube, but this drops to 30% in the case of the low-mass galaxy NGC 5068.

3.2. *Spatial scales, convolution, and clipping*

We compare the distributions of CO and Hα at a series of common spatial resolutions up to 1.5 kpc. The best physical resolution shared by our entire sample is 140 pc, which is set by the resolution of our CO map of NGC4254. We adopt 140 pc as the fiducial measurement scale for our analysis.

To convolve the data, we smooth the thresholded images using Gaussian convolution kernels. For each convolved map, we sort the map pixels by intensity (from brightest to faintest), and reject the faintest pixels that together contribute 2% of the total flux. We verified that this additional clipping level is sufficient to remove faint halos that are convolution artifacts. This step sets a large amount of area to have zero intensity at each scale without significantly affecting the flux in the analysis. We tested that other reasonable rejection criteria (between 1 and 5%) do not affect our conclusions.

Finally, we note that while we apply the same methodology to the CO and Hα maps, the output depends on the intrinsic distribution of the emission in the input map. Faint emission located next to a bright peak in the input map will tend to be recovered in the lower resolution map, for example, while isolated faint emission is more likely to fall beneath the 2% clipping threshold in the lower resolution maps. In this sense, our smooth-and-clip strategy is likely to impact our CO and Hα maps differently. Our method for DIG removal often results in high-brightness regions being surrounded by zero-valued pixels. On the other hand, the mass surface density threshold applied to construct our CO maps tends to yield contiguous regions of relatively faint emission. We note this as another potential area for improvement.

3.3. *Measurements*

Using the pairs of matching resolution CO and Hα maps, we classify each pixel into one of four categories:

- ***CO only*** – only CO emission is present, Hα emission is not detected at this position and scale.
- ***Hα only*** – only Hα emission is present, CO emission is not detected at this position and scale.
- ***Overlap*** – both CO and Hα emission are present.
- ***Empty*** – neither CO nor Hα emission are present.

This classification is scale dependent, e.g., a pixel may be classed as *empty* at high resolution, *CO only* at intermediate resolution, and *overlap* at low resolution. At high resolution, a non-negligible fraction (on average around 60-70%) of pixels falls in the last category (see Fig. 2), indicating that large areas of galaxy disks are not directly filled with star-forming ISM. At coarse resolution, the number of empty pixels decreases significantly, giving the impression that the star-forming ISM is ubiquitous. The differences among distributions of empty pixels among galaxy disks is thus a potentially interesting diagnostic of ISM evolution and galaxy morphology. In this paper, however, we are most interested in the impact of host galaxy properties and observing scale on the relative configuration of the molecular and ionized gas phases, so we do not analyse the fraction of empty pixels in detail.

At each spatial scale after removing the empty pixels, we calculate the fraction of pixels in each of the first three categories, i.e. with a detection of CO, Hα or both. At fixed scale, these fractions may be plotted as a pie chart (Section 4.1). The evolution of these fractions as a function of scale can be illustrated using a bar graph (Section 4.2).

To assess the uncertainty on our measurements, we repeated our analysis while varying the thresholds for CO

Table 3. Line of Sight Fractions at 140 pc Scale.

Name	CO only (%)	Hα only (%)	overlap (%)
NGC0628	42^{54}_{27}	19^{32}_{12}	38^{42}_{34}
NGC3351	15^{35}_{8}	66^{81}_{63}	19^{24}_{13}
NGC3627	40^{47}_{33}	17^{25}_{10}	43^{49}_{37}
NGC4254	52^{67}_{39}	11^{17}_{6}	37^{43}_{28}
NGC4321	41^{53}_{29}	27^{40}_{18}	32^{38}_{23}
NGC4535	46^{61}_{37}	23^{38}_{13}	31^{37}_{26}
NGC5068	2^{7}_{1}	86^{90}_{73}	12^{20}_{10}
NGC5194	55^{59}_{52}	6^{8}_{4}	38^{39}_{35}
Median	42	23	37
Mean	37	32	31

NOTE—Fraction of sightlines with CO emission only, Hα emission only, and both CO and Hα emission. These fractions represent the numbers corresponding to the pie charts shown in Fig. 3. The sub- and super-scripts correspond to the minimum and maximum values obtained when different thresholds for positive detection of CO emission and DIG suppression are used (see text). The mean (median) values reported in the final row are the means (medians) of our fiducial measurements reported for a given sightline category. Note that the medians are not re-normalized, thus the sum will not add up to 100%.

and Hα flux. We tested varying the CO threshold between 10 and 15$M_\odot$ pc^{-2} at 140 pc scale, and thresholding at the native resolution of the CO maps using signal-to-noise criteria (i.e. 3 and 5σ cuts in integrated intensity). We also varied the unsharp masking parameters used for DIG removal, varying the size of the smoothing kernels by 25%, the gain in the first subtraction step by 25%, and the signal-to-noise threshold of the mask by $\pm1\sigma$. We adopt the minimum and maximum values of the pixel fractions obtained from this suite of tests as an indication in the uncertainty of our measurements.

4. RESULTS

Following the methodology in §3, we measure the fraction of detected sightlines with Hα emission, CO emission, or both at each spatial scale. For plots in this section, sightlines with *Hα only* emission are shaded with red tones, sightlines with *CO only* emission are shaded with dark blue tones, and sightlines with overlapping CO and Hα emission (*overlap*) are shaded with lavender tones.

4.1. *CO and Hα at 140 pc resolution*

Fig. 2 shows results for all galaxies at 140 pc resolution in map form. Table 3 summarizes the statistics for these maps, and Fig. 3 visualizes these statistics as pie charts. Following §3, the error bars in Table 3 show the effect of varying our CO and Hα detection thresholds across their plausible ranges.

At this resolution, emission from one or both of these tracers is typically present across 50% or more of our survey area. Of the detected sightlines, *CO only* sightlines (dark blue) are the most common detections in more than half of our targets (namely NGC 0628, NGC 4254, NGC 4321, NGC 4535, NGC 5194). In two targets *Hα only* sightlines dominate (NGC 3351 and NGC 5068). NGC 3627 – the most inclined galaxy in our sample with $i \sim 55°$ – is our only target where sightlines with *overlapping* CO and Hα emission are the most common.

Across the sample, the median fraction of detected sightlines that contain *CO only* emission is ∼40%. This is comparable to the fraction of *overlap* sightlines (∼ 40%), while the fraction of *Hα only* sightlines is typically only ∼ 20%. The clear separation of the CO and Hα emission at our high working resolution (i.e., the lower overlap fraction compared to sightlines with one tracer only), and the detection of widespread CO emission above 12.6 $M_\odot$ *pc*$^{-2}$ without associated Hα emission (typically *CO only* sightlines are more than 2× more abundant than *Hα only* ones) are two main results of this paper.

Table 4 (see also Fig. 9) shows the results when we consider how the CO and Hα *fluxes* (rather than the number of sightlines) are distributed between different categories, i.e. instead of the number of pixels in each category, we consider their respective contribution to the total CO or Hα flux. On average, we find that ∼ 40% of the CO flux at 140 pc resolution remains unassociated with bright Hα emission. This is lower than the ∼ 60% of *CO only* sightlines, but implies the same qualitative conclusion that there is a significant mass fraction of CO-traced molecular gas without Hα emission.

We find a greater discrepancy between the distributions of flux and sightlines for Hα. At our fiducial 140 pc scale, the median *overlap* fraction for Hα emitting sightlines is about two-thirds across our sample. These same regions contribute a median of ∼ 80% of the total Hα flux. These results indicate that these *overlap* sightlines, which show both CO and Hα, tend to have higher Hα intensity than sightlines probing *Hα only* emission. This agrees with a visual inspection of the maps. Since these *overlap* regions are by definition co-spatial with CO-emitting molecular gas, they likely suffer from dust attenuation that we do not account for in the processing of our Hα maps (c.f. § 2.2.4 and 2.2.6). The true flux contribution of these regions is thus probably higher than the ∼ 80% that we measure.

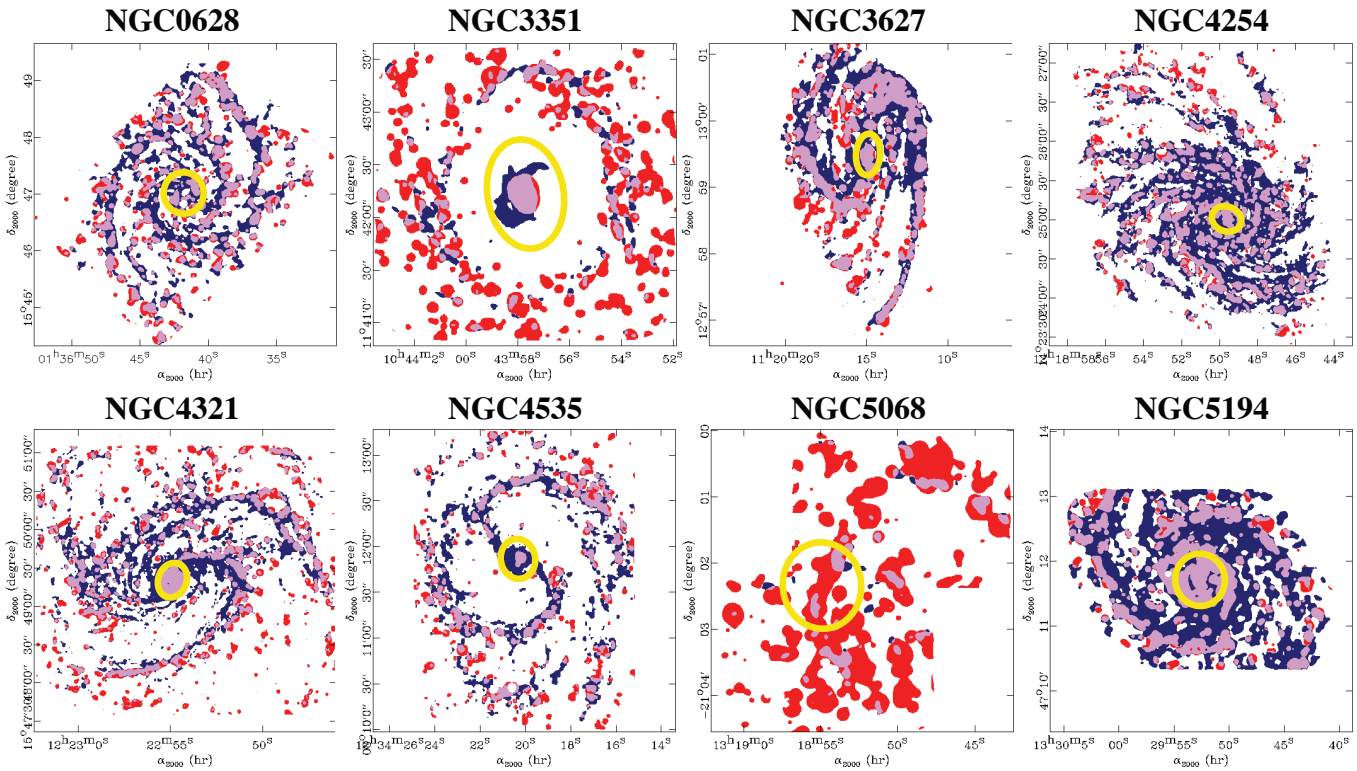

Figure 2. Galaxy maps showing regions with *overlapping* CO and Hα emission (lavender), *CO only* emission (dark blue) and *Hα only* emission (red) at a spatial resolution of 140 pc for our sample. The region that we define as the galaxy center is indicated in each panel as a yellow ellipse.

Galaxy centers can contribute significantly to the total flux while covering only a few sightlines. Fig. 2 and Fig. 1 show that the galaxy centers in our sample tend to have *overlapping* high intensity CO and Hα emission. In § A, we test the degree to which the centers drive the discrepancies between our flux- and sightline-based measurements. To do this, we repeated the calculation considering only the main galaxy disks, i.e., excluding the region within a radius of 1 kpc of the reference position listed in Table 1 for all galaxies. For NGC 3351, we follow Sun et al. (2018) who adopted a larger radius of 1.5 kpc so that the visually distinct inner disk is entirely inside the central region of NGC 3351. The regions that we define as central are indicated by yellow ellipses in Fig. 2. Excluding the central regions from our analysis improves the agreement between the flux- and sightline-based measurements for NGC 3351, but does not significantly alter our results for other galaxies.

Relation to morphology – In most galaxies, the CO emitting sightlines form coherent, kiloparsec-scale structures such as spiral arms, bars, or rings in the disk. The sightlines probing Hα emission appear more irregular and patchy than the CO emission, though they generally trace out the same galactic structures as the CO. *Overlap* sightlines with both CO and Hα emission appear prevalent in the centers of almost all targets (indicated by the yellow ellipse in Fig. 2) and along the major galactic structures traced by CO emission.

In several galaxies with strong spiral arms, we find a pronounced offset between sightlines probing Hα emission and those with *CO only*. This is most evident along the spiral arms of NGC 0628, NGC 4321, and NGC 5194, but the same pattern can be seen in NGC 4254, and NGC 4535. The sense of the offset is that the sightlines with Hα (*both overlap and Hα only*) tend to lie along the convex side of the arm, offset from the *CO only* ones. Assuming that the spiral arms are trailing, this implies that the *Hα only* and *overlap* sightlines appear offset downstream from the *CO only* sightlines (when observing them inside their co-rotation).

The overlap in the central regions appears strong for the barred galaxies NGC 3351, NGC 3627, NGC 4321, and NGC 4535. In several of these targets, we see *overlapping* CO and Hα in the central region, and then again in the region outside the stellar bar. Along the bar itself, we see predominantly *CO only* emission, though this emission is not always present along the full length of the bar (e.g., see NGC 3351). A similar feature appears in NGC 5194, with *CO only* sightlines appearing along segments of the inner spiral arms (features associated with strong streaming motions by Meidt et al. 2013).

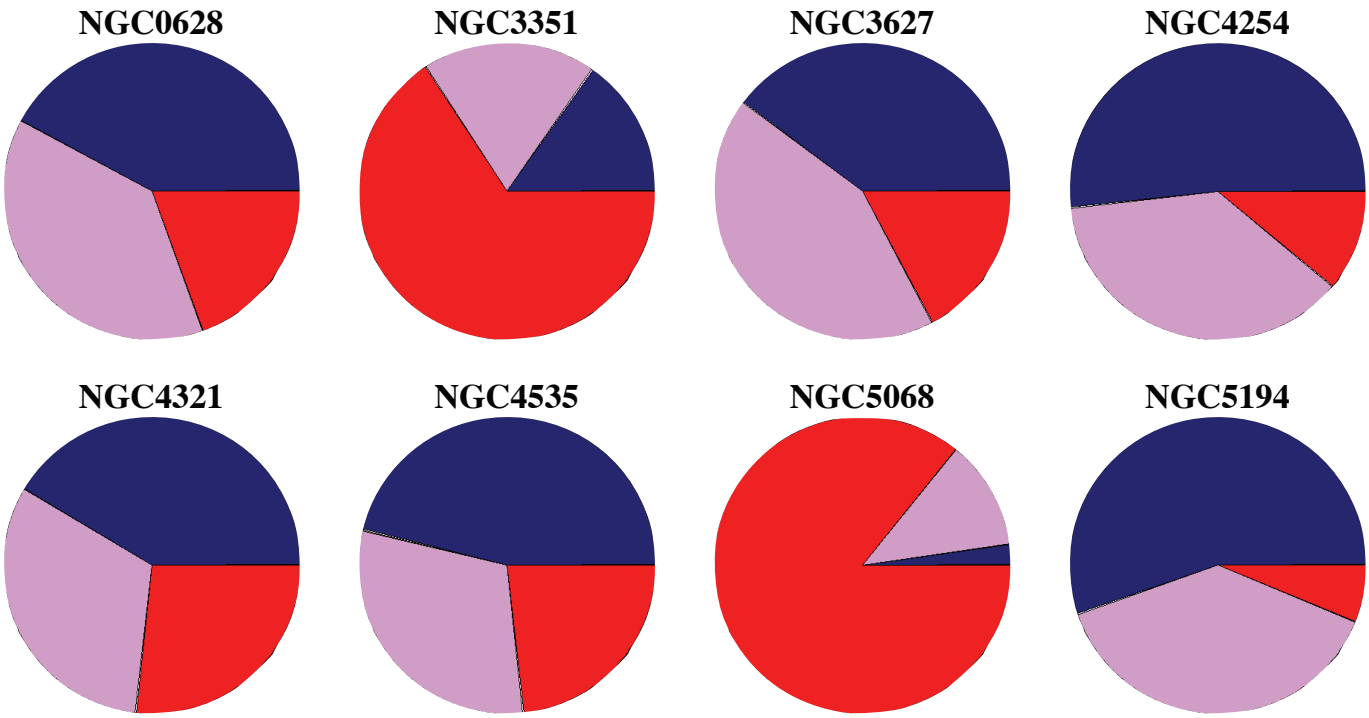

Figure 3. Pie charts indicating the fraction of sightlines with CO and Hα emission for the 140 pc resolution maps of our eight galaxies (from *left* to *right*: NGC 0628, NGC 3351, NGC 3627 and NGC 4254, *(top row)*; ; and NGC 4321, NGC 4535, NGC 5068, NGC 5194 *(bottom row)*). The color coding is dark blue – *CO only*, red – *Hα only*, lavender – *overlap*.

Here and throughout our analysis, NGC 5068 shows a distinct morphology: a patchy, incoherent distribution of CO and Hα emitting regions. This galaxy has the lowest stellar mass, lowest metallicity and latest Hubble type in our sample. It resembles M33, NGC 300 and the Large Magellanic Cloud, where similar observations have found tracers of gas and star formation to be incoherent on small scales (Kawamura et al. 2009; Schruba et al. 2010; Onodera et al. 2010; Gratier et al. 2012; Faesi et al. 2014). Those studies have postulated that star formation in dwarf spirals proceeds in a stochastic way, without any large-scale organization.

Trend with Galactocentric Radius – Visual inspection of the maps in Figure 2 suggests that many of the *Hα only* sightlines occur towards the outer edges of our maps. We quantify this in Figure 4, where we plot the *CO only*, *Hα only* and *overlap* fractions in annuli of width $0.2R_{25}$. Indeed in all galaxies except NGC 5068, there is a clear trend for the *Hα only* fraction to increase with increasing galactocentric radius. This increase seems more pronounced in barred galaxies (plotted with circles and solid lines in Figure 4). At the same time the radial distribution of the *CO* sightlines (both *CO only* and *overlap*) shows on average a stronger (decreasing) trend for barred galaxies than for the three non-barred ones, however, also with a much wider spread in values. A possible explanation for these trends is the fact that photoionization bubbles expand more quickly in low-density media because the Strömgren radius scales as $\rho^{-2/3}$, thus larger HII regions are expected at larger radii where the gas surface density is presumably lower. Conversely, this decrease in gas surface density should lead to more isolated patches of molecular gas. As many other galaxy parameters vary with galactocentric radius, e.g., metallicity, a secure interpretation of these trends requires further investigation using a larger sample with better sampling of galaxy morphological type and stellar mass.

4.2. *Overlap between CO and Hα as function of spatial scale*

Figs. 5 and 6 illustrate the spatial distribution of CO and Hα emission as we vary the resolution of the maps (showing maps at 140 pc, 300 pc, 500 pc, and 1000 pc). In Figs. 7 and 8, we plot the covering fractions of *CO only*, *Hα only*, and *overlap* regions as a function of spatial scale (from 140 pc up to 1.5 kpc in steps of 100 pc starting at 200 pc).

From 140 pc to 500 pc resolution – As we blur the maps from 140 pc to 500 pc resolution, sightlines where CO and Hα emission coincide become more prevalent in all galaxies. By 500 pc resolution, *overlapping* (lavender) sightlines dominate (>60%) while *CO only* sightlines make up <25% of the emitting sightlines in all targets. For most targets, we see a significant slow-down in the

Table 4. Line of Sight and Flux Fractions per Tracer at 140 pc Scale.

	By Number				By Flux			
	CO Sightlines		Hα Sightlines		CO Flux		Hα Flux	
Name	CO only	CO overlap	Hα only	Hα overlap	CO only	CO overlap	Hα only	Hα overlap
	(%)	(%)	(%)	(%)	(%)	(%)	(%)	(%)
NGC0628	52	48	34	66	43	57	18	82
NGC3351	44	56	77	23	21	79	24	76
NGC3627	48	52	29	71	31	69	12	88
NGC4254	58	42	23	77	45	55	11	89

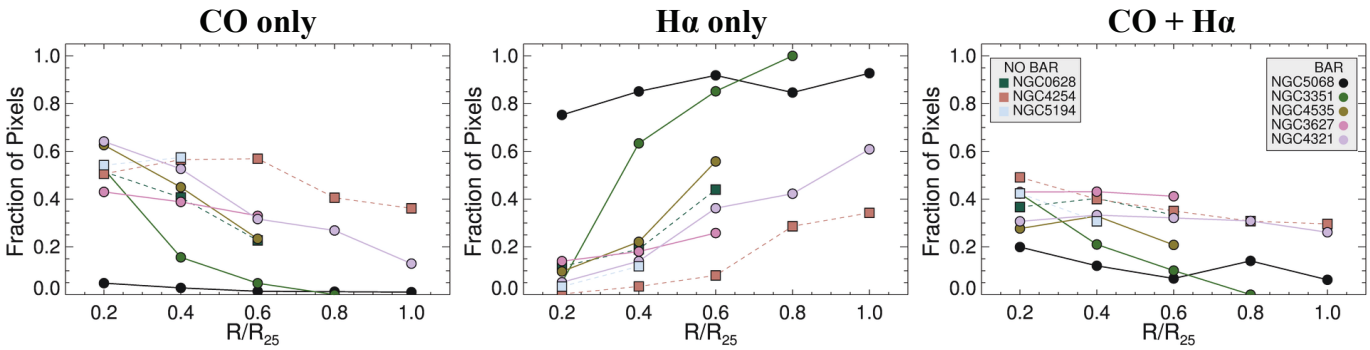

Figure 4. Variation of the overlap fraction at 140 pc resolution as a function of galactocentric radius. The x-axis is normalized by R_{25}, and the curves are color-coded by increasing stellar mass. Barred galaxies are shown with circles and solid lines, non-barred galaxies with squares and dashed curves. The classification of Tab. 1 is adopted.

increase of the fraction of *CO only* sightlines at spatial scales of ∼150-200 pc. The exceptions are NGC 4254 and NGC 5194, where the *CO only* fraction continuously decreases from 140 pc to larger scales.

Most of the evolution of *overlap* fraction and structure of *CO only* emission occurs over this range, 140−500 pc. As the resolution degrades, the detailed morphology visible at high resolution evolves toward a simple, amorphous geometry. Structures that were prominent at sharper resolution, such as spiral arms and bars, disappear and emission fills in the region between galactic structures. As this happens, the region covered by *overlapping* CO and Hα emission grows from patches to form coherent structures along spiral arms and stellar bars. Over this range, in all but two galaxies (NGC 3351 and NGC 5068) the *Hα only* covering fraction shows less significant evolution than the *CO only* or *overlap* fraction. Three-quarters of our sample show no variation in *Hα only* covering fraction for scales of 300 pc and larger. In these cases, the *Hα only* regions often appear as mostly isolated, compact regions, often located at large galactocentric radius.

Beyond 500 pc resolution – As we blur the maps to resolutions greater than 500 pc, the *overlap* sightlines tend to become unified structures that include the galaxy nucleus. By 1.0 kpc resolution, the *CO only* (dark blue) sightlines tend to no longer trace galactic structures, but rather appear spread across the galaxy. This heavy overlap between CO and Hα emission at coarse resolution agrees with numerous previous studies showing a tight correlation between these quantities at this resolution (e.g., Bigiel et al. 2008; Leroy et al. 2008; Liu et al. 2011; Leroy et al. 2013; Bolatto et al. 2017).

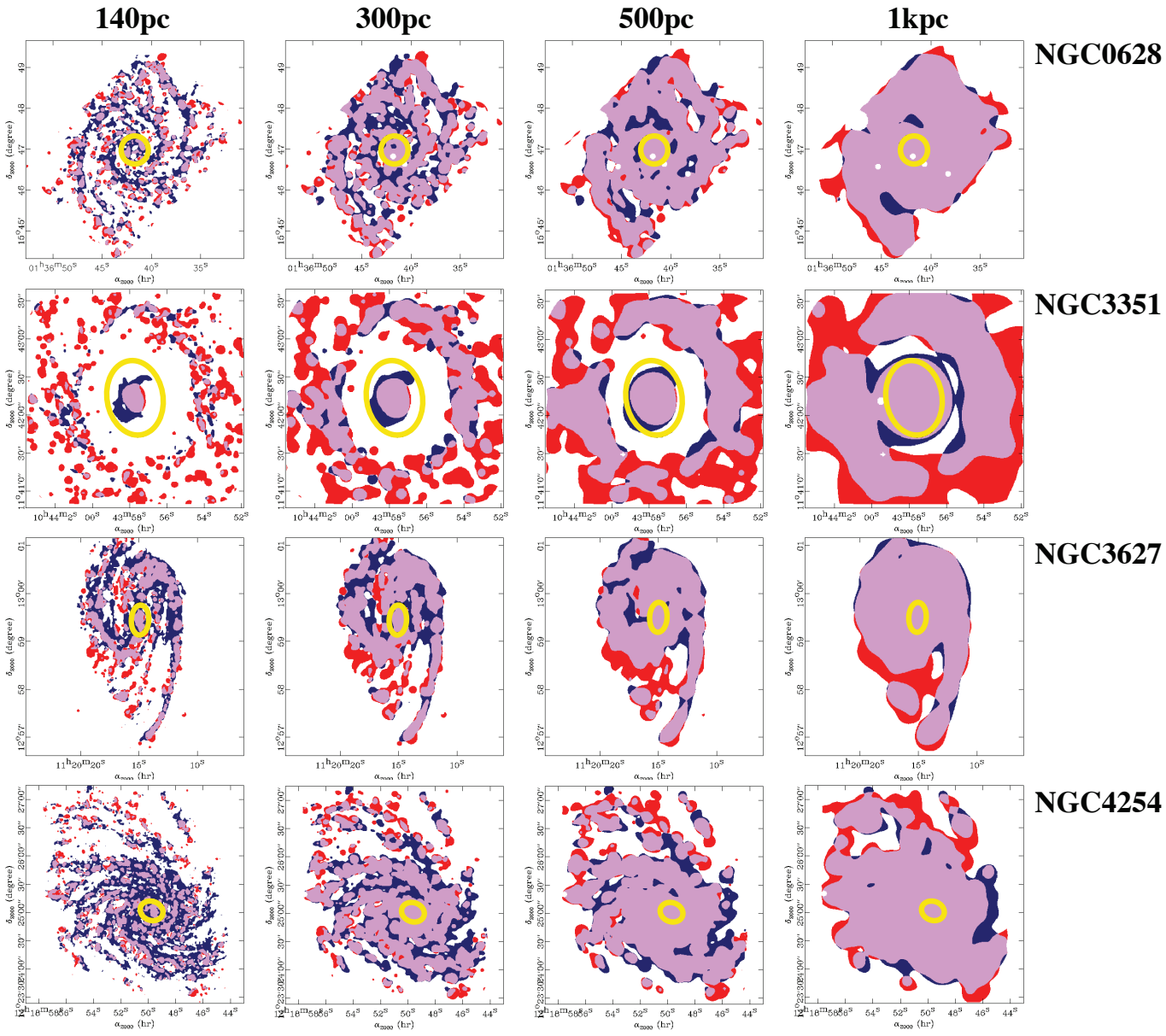

Figure 5. Galaxy maps showing regions with overlapping CO and Hα emission (lavender), *CO only* (dark blue) and *Hα only* emission CO (red) at spatial resolutions of 140, 300 and 500 and 1000 pc (*left to right*) for NGC 628, NGC 3351, NGC 3627 and NGC 4254.(*top to bottom*).

Overall, the changes in morphology and covering fraction beyond 500 pc resolution appear less pronounced than those between 140 pc and 500 pc. For the majority of our sample, the most significant changes in the fraction of *overlapping* (lavender) sightlines occur between 140 and 500 pc resolution. The fact that this overlap emerges only after averaging agrees with previous observations of increasing scatter in the correlation between molecular gas and star formation tracers with decreasing spatial scale (e.g., Bigiel et al. 2008; Schruba et al. 2010; Onodera et al. 2010; Leroy et al. 2013; Kruijssen et al. 2019).

5. DISCUSSION

We have analyzed a sample of matched resolution, high completeness, wide area CO and Hα maps, which trace molecular gas and high-mass star formation. Consistent with previous observational studies targeting individual galaxies (e.g. M33 and M51, Schruba et al. 2010; Meidt et al. 2013), we find a large reservoir of molecular gas not directly associated with high-mass star formation at high spatial resolution. A significant non-star-forming molecular gas reservoir in galaxies is expected from numerical simulations (e.g. Semenov et al. 2017). This component has been almost impossible to

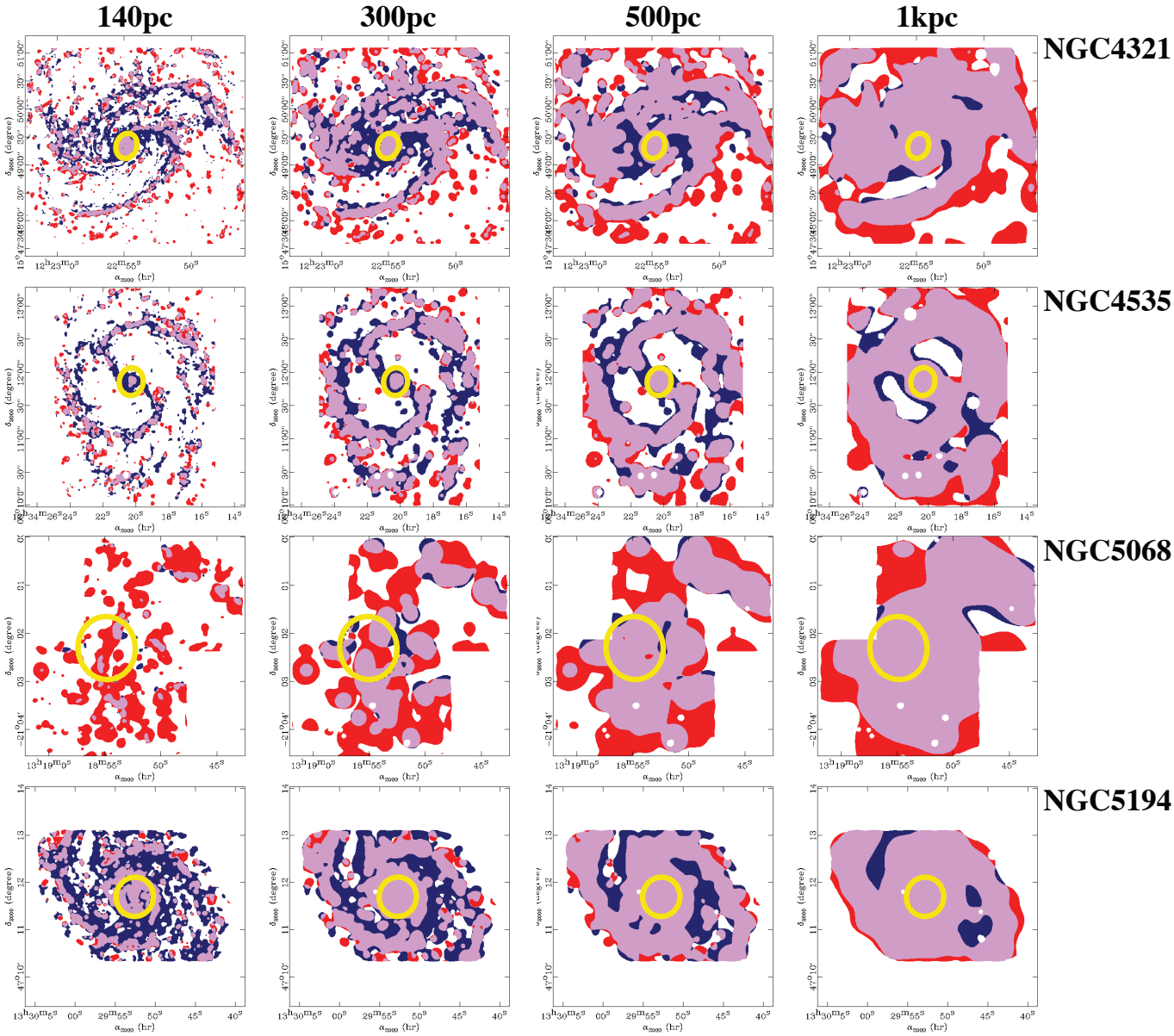

Figure 6. Galaxy maps for NGC 4321, NGC 4535, NGC 5068 and NGC 5194 (*top to bottom*). (For details see caption of Fig. 5.)

identify in previous, low resolution surveys because the apparent overlap between tracers of molecular gas and star formation increases with degrading resolution. At the coarsest resolutions that we study, $\sim 1.0 - 1.5$ kpc, CO and Hα emission appear almost completely coincident.

We also clearly observe the effects of galactic dynamics in the maps: bars, spiral arms, and central regions all stand out in our analysis. This dynamically-induced complexity indicates that the timescales associated with different steps in the star formation process (e.g. cloud formation, cloud dispersal) may depend on galactic environment. We thus expect timescale estimates based on galaxy-wide measurements and simple cycling arguments to mask intrinsic variation of star formation timescales within galaxies.

With this caveat in mind, we derive rough estimates for the time required for the molecular gas in our sample galaxies to cycle between a quiescent and actively star-forming state (see §5.2). Our measurements imply that this timescale is ~ 1 to 2 times longer than the characteristic lifetime of an HII region. This is broadly consistent with estimates for molecular cloud lifetimes, but much shorter than the global molecular gas depletion times of ~ 2 Gyr observed for nearby galaxies (Leroy et al. 2008). An investigation of molecular cloud lifetimes across a subset of PHANGS galaxies using an alternative formalism is presented by Chevance et al. (subm.).

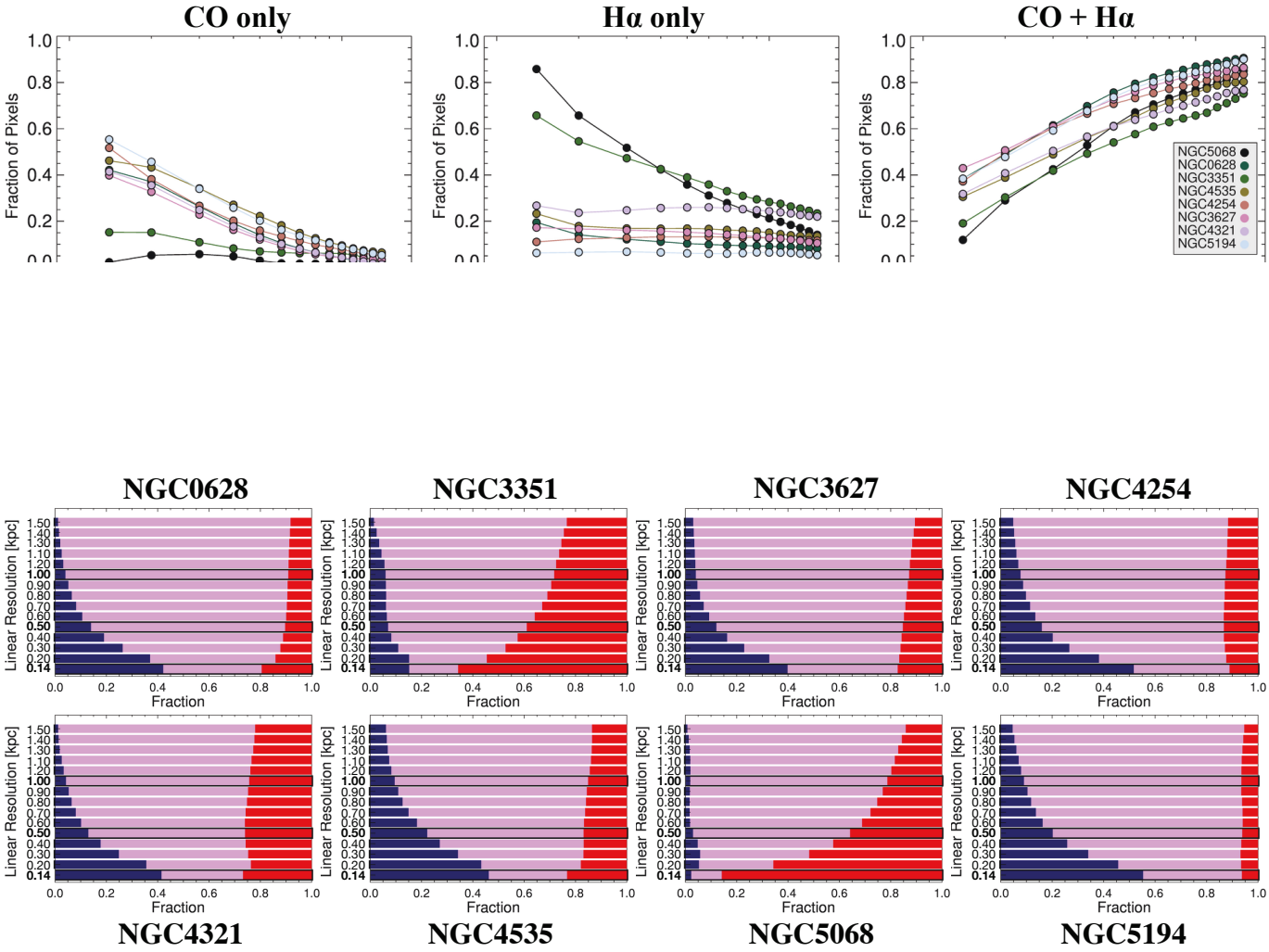

Figure 8. Bar graphs indicating the fraction of sightlines with CO and Hα emission across the range of spatial scales that we explore. The order of the galaxies and the color code are the same as for Fig. 3. The spatial scales of 140pc, 500pc and 1kpc are highlighted by a black outline.

5.1. *Quiescent molecular gas at high resolution, overlap at low resolution*

The relative contributions of *CO only*, *Hα only* and *overlap* sightlines vary dramatically with spatial scale. At ~ 140 pc resolution, we find a roughly equal number of CO-emitting sightlines (at and above our H_2 surface density threshold of $12.6\,M_\odot pc^{-2}$) with and without associated Hα emission in our sample galaxies. The *CO only* sightlines contribute $\sim 40\%$ of the total CO flux above this threshold. This implies the presence of a significant reservoir of quiescent molecular gas.

This apparently quiescent molecular gas could have several distinct physical origins. This gas may be genuinely non-star-forming, due to large-scale dynamical effects that stabilize the gas (e.g., Meidt et al. 2013, subm.) or the disruptive effect of stellar feedback (e.g. Krumholz, & McKee 2005; Ostriker et al. 2010). Alternatively, it could be forming stars that are not massive enough to generate the ionizing photons needed for significant Hα emission. High-mass stars could be forming behind a screen of dust that obscures Hα photons (see Table 2). Or the gas could still be in the process of collapsing, reflecting recently formed molecular clouds that have not yet "ramped up" star formation (e.g., Lee et al. 2016).

Quiescent gas and spatial scale: This quiescent molecular gas is only accessible thanks to the high physical resolution of our data. For our adopted CO and Hα thresholds, the fraction of *CO only* sightlines decreases from $\sim 40\%$ at 140 pc resolution to $\lesssim 15\%$ at 500 pc. Our adopted fiducial scale of 140 pc is a pragmatic choice, not a physical one. For five galaxies in our sample, the best matching spatial resolution of our data is 90 pc or better, allowing us to test whether the fraction of *CO only* sightlines in galaxies is larger at higher physical resolution. We repeated the analysis described

in Section 3 for the CO and Hα maps of these galaxies at 90 pc resolution, using a threshold of 19.5 $M_\odot pc^{-2}$ (i.e. the 3σ mass surface density sensitivity of our NGC 5194 data at 90 pc resolution). We find that the fraction of *CO only* sightlines in all galaxies shows a relative increase of 5 to 20% as the resolution improves from 140 to 90 pc. The fraction of *Hα only* sightlines typically shows a similar relative increase, while the fraction of *overlap* sightlines shows a relative decrease of $\sim$ 30% as the resolution improves.

At coarser resolution than 140 pc, the quiescent CO emission rapidly vanishes as the resolution is degraded. The rapid decrease in *CO only* sightlines between 140 and 500 pc resolution is accompanied by a significant increase in the fraction of *overlap* sightlines (from $\sim$ 30% to $\sim$ 65%) across this range of scales.

For most of our sample, the visible morphology of CO emission also changes over this spatial range: as the resolution degrades, the initially sparse, patchy *overlap* sightlines become more common, while the *overlap* regions spread out, replacing the *CO only* regions and covering the main morphological features of the galaxy. Scale-dependent variations in the fraction and spatial distribution of the *Hα only* sightlines are less marked in our current, small sample of galaxies. This is because the *Hα only* regions tend to be relatively isolated, distinct regions towards the outer parts of our maps.

At resolution coarser than $\sim$ 500 pc, the *overlap* sightlines cover most of the mapped area in all targets. At these scales, differences in the morphology of the CO and Hα emission disappear. Even major morphological features of galaxies (e.g., prominent spiral arms, very luminous H II regions in outer disks) start to "wash out" and are mostly indistinguishable on spatial scales above $\gtrsim$1.0 kpc.

Our results agree with previous observations showing how star formation scaling relations – i.e. the power law scaling between the molecular gas and star formation rate (SFR) surface density, where SFR is typically traced by Hα emission – vary with spatial scale. Several studies have demonstrated that the scatter in the molecular gas depletion time decreases as the spatial scale of the molecular gas and SFR surface density measurements increases. These works include high resolution studies of individual galaxies (e.g. Blanc et al. 2009; Schruba et al. 2010; Onodera et al. 2010; Kreckel et al. 2018; Kruijssen et al. 2019) and coarser resolution studies of larger galaxy samples (Bigiel et al. 2008; Leroy et al. 2013). To our knowledge, our work here represents the best combination of resolution (140 pc across the sample) and sample size (8 galaxies) to date.

Table 5. Inferred Relative Gas Cycling Timescales by Sightlines at Various Scales.

Name	$f_{scale} = \frac{f_{CO-only}+f_{overlap}}{f_{H\alpha-only}+f_{overlap}}$			
	140 pc	300 pc	500 pc	1000 pc
NGC 0628	1.4	1.2	1.0	0.9
NGC 3351	0.4	0.6	0.7	0.8
NGC 3627	1.4	1.1	1.0	0.9
NGC 4254	1.8	1.2	1.0	0.9
NGC 4321	1.3	1.0	0.9	0.8
NGC 4535	1.4	1.3	1.1	0.9
NGC 5068	0.1	0.5	0.7	0.8
NGC 5194	2.1	1.4	1.2	1.0
Median	1.4	1.2	1.0	0.9
Mean	1.2	1.0	1.0	0.9

NOTE—**The reported values are derived using Eq. 1 and need to be multiplied by the assumed $t_{H\alpha}$, i.e. the time an HII region is visible above our thresholds.** See text for discussion of reasonable values for $t_{H\alpha}$.

5.2. *Temporal interpretations*

Under the assumption of simple steady-state cycling, every star-forming unit progresses from a cold gas cloud that is not yet forming stars (*CO only*) to a cold gas cloud that is actively forming massive stars (*overlap* regions) to a region of massive young stars from which the cold gas has been entirely dispersed (*Hα only*). In this case, the covering fractions that we measure are a reflection of the time spent by a star-forming region in each of these different evolutionary phases.

Versions of this steady-state cycling heuristic have been used by Kawamura et al. (2009) to estimate the lifetimes of molecular clouds in the LMC, and by Gratier et al. (2012) and Corbelli et al. (2017) to characterize the cloud life-cycle in M 33. Recently, Battersby et al. (2017) applied a similar approach to Milky Way observations to determine the timescales for dense molecular gas structures (i.e. clumps) to evolve from starless to star-forming. Schruba et al. (2010) invoked a similar cycling scenario to explain the scatter and bias in the molecular gas depletion time measured at high spatial resolution in M 33. Feldmann et al. (2011) also considered this phenomenon in terms of the scatter (see also Leroy et al. 2013). Building on this work, Kruijssen & Longmore (2014) and Kruijssen et al. (2018) developed a general formalism to derive the evolutionary timescales of star-forming regions from concentric apertures centered on peaks identified at different wavelengths. This formalism has been applied to CO and Hα maps of the spiral galaxy NGC 300, an M 33 analog, in order to estimate the typical lifetime of molecular clouds and character-

istic duration of star formation feedback in that galaxy (Kruijssen et al. 2019). Analogous arguments have been used to infer timescales in other fields, including, e.g., to measure the life cycle of protostars (e.g., see review in Dunham et al. 2014). All these methods require an externally calibrated fiducial clock, e.g., the time $t_{H\alpha}$ over which an HII region is visible, to translate between population/mass/area statistics and an absolute timescale.

Here we apply a simple version of this approach to molecular gas that is visible above a fixed surface density threshold, treating individual pixels as discrete star-forming units. The lifetime of the cold molecular gas in a star-forming unit is then

$$t_{gas} = t_{H\alpha} \times \frac{f_{CO-only} + f_{overlap}}{f_{\mathrm{H}\alpha-only} + f_{overlap}} = t_{H\alpha} \times f_{scale} \ , \quad (1)$$

where f_{CO} is the fraction of *CO only* sightlines, $f_{H\alpha}$ the fraction of *Hα only* sightlines, and $f_{overlap}$ the fraction of *overlap* sightlines. Then f_{scale} represents the scaling factor to translate from the fiducial timescale, here $t_{H\alpha}$, to the lifetime for a cold gas structure.

5.2.1. *Timescales*

Table 5 reports the results of Eq. 1 applied to our sample at various scales using the numbers derived in § 4. As the resolution improves (i.e., the spatial scale decreases), regions with *overlapping* Hα and CO emission tend to occupy a diminishing fraction of sightlines (see Fig. 8). The ratio f_{scale} thus tends to increase for galaxies where *CO only* sightlines are prominent, while it decreases rapidly for galaxies where *Hα only* sightlines dominate (i.e., NGC 3351 and NGC 5068). If we were to improve upon our 140 pc resolution, we would expect these trends to continue. This highlights some natural next steps to improve on the current data treatment (see § 5.5).

For most of our targets, these measurements imply a median CO visibility timescale of 1.4× the Hα visibility timescale $t_{H\alpha}$ at 140 pc resolution. Typical estimates for the visibility time of Hα are 5−10 Myr[6]. Binaries, extinction, and other effects may complicate the picture, but taking these numbers at face value, Table 5 suggests molecular cloud lifetimes of ∼ 10−15 Myr at our best resolution of 140 pc.

While there is a clear dependence on scale (and the data have some limitations, see § 5.5), these short timescales are in reasonable agreement with measurements of molecular cloud lifetimes in other galaxies in the literature (see above). For the specific galaxies in our sample besides NGC 5068 and NGC 3351, our estimates also agree within a factor of ∼ 2 with cloud timescale estimates obtained by Chevance et al. (subm.) applying the formalism of Kruijssen et al. (2018) to these systems. This robustness to adopted methodology suggests that both sets of results do indeed reflect the true underlying cycling times.

The order of magnitude of t_{gas} also agrees well with theoretical estimates of the timescale for star formation. It is comparable to the crossing or free-fall time for individual molecular clouds (e.g., see Heyer et al. 2009; Fukui, & Kawamura 2010, for typical cloud properties), including those in our sample (e.g., see Utomo et al. 2018, for direct estimates). Many models have taken either the crossing time (e.g., Elmegreen 2000) or the free-fall time (e.g., Krumholz, & McKee 2005) as the relevant timescale for star formation. Numerical models find similar results, e.g., based on recent highly resolved simulations of galaxy disks, Semenov et al. (2018) quote star formation timescales of ∼5-15 Myr. Our measurements support the idea that the onset of star formation and dispersal of clouds occurs over roughly this timescale.

5.2.2. *A more dynamic view*

The simple evolutionary sketch underlying Equation 1 may be too simple to capture the evolution of real regions in the molecular ISM. Recent numerical simulations of galaxies suggest that molecular gas may cycle in and out of a bound, cloud-like state several times before finally participating in the formation of stars (e.g. Dobbs et al. 2015; Semenov et al. 2017), and that this may explain the discrepancy between the molecular gas depletion times measured for entire galaxies (∼ 2 Gyr, e.g. Leroy et al. 2008) and individual molecular clouds (a few hundred Myr, e.g. Evans et al. 2009; Heiderman et al. 2010). In this case, not every patch of visible CO emission will form stars in the near future.

Moreover, grouping together CO-bright stellar bars and Hα-bright regions at large galactocentric radius will not capture local, physical cycling between gas and star formation. Even in star-forming regions, the visible CO-Hα offsets associated with spiral arms (e.g., prominently observed in M 51, see e.g. Schinnerer et al. 2013, 2017) suggest that a one-dimensional flow model (e.g., Meidt et al. 2015; Dobbs, & Pringle 2013) may be more appropriate than stochastic cycling.

The trends of decreasing f_{scale} with increasing resolution for 6 of our 8 galaxies might also reflect this more dynamic view. For example, in the Semenov et

[6] Based on population synthesis models, Kennicutt & Evans (2012) estimate that 90% of emission is emitted within ∼ 10 Myr with a mean age of ∼ 3 Myr for the associated stellar population (for other estimates, see, e.g. Leroy et al. 2012; Haydon et al. 2018).

al. (2017) model, gas cycles in and out of a star-forming state several times before a fraction of the star-forming gas is converted into stars. Thus with increasing resolution we start to probe gas cycling between a star-forming and non-star-forming state which is setting the timescale t_{gas} we infer. The inverse trend in f_{scale} observed for especially NGC 5068 and potentially NGC 3351 may be set by their rather short timescale for *localized* star formation to occur. This timescale is set by stellar feedback that quickly removes gas from the star-forming state (see also, e.g., Kruijssen et al. 2019) and such galaxies are in the "self-regulation" regime.

5.3. *Visible effects of galactic dynamics*

Our maps show clear signatures of galactic dynamics. In addition to the high overlap fraction in most galaxy nuclei, we observe signatures of the suppression of star formation in bars and offsets between Hα and molecular gas emission along spiral arms.

Central regions: All our eight galaxies show prominent *overlap* regions in the central 1 kpc (see Fig. 5). Close inspection of the CO intensity maps and Hα images presented in Fig. 1 suggests that the overlap is arising mainly due to Hα emission related to (a) central star formation mostly distributed in so-called nuclear star-forming rings (e.g. NGC 3351 and NGC 4321 are listed in the AINUR catalog of Comerón et al. 2010) or along the stellar bar (in NGC 5068) or (b) the presence of AGN (e.g., as good examples see NGC 3627, NGC 5194) where the Hα emission is coming from the ionized gas in the narrow line region (e.g. in NGC 5194; Blanc et al. 2009). Thus, unlike the Central Molecular Zone (CMZ) in our own Galaxy, other nearby galaxies can show significant star formation, especially in the nuclear star-forming rings that are typically found in barred galaxies (see also review by Kennicutt 1998b). Our inability to discriminate between Hα emission arising from truly star-forming structures or from a central AGN is a caveat for the interpretation of our results in galaxy centers (see § 5.4 for further discussion).

Stellar bars: Observational and theoretical work on the role of stellar bars in star formation still draws somewhat conflicting conclusions about the roles for these structures. It is clear that bars help drive material to the central regions of galaxies, but whether they enhance or suppress star formation along the way remains debated (e.g., see Meidt et al. 2013; Renaud et al. 2016; James & Percival 2018). Two of our targets, NGC 3351 and NGC 4535, show strong signatures of suppressed star formation along a strong stellar bar. Two more, NGC 3627 and NGC 4321 show some evidence of this phenomenon.

The signatures are a clear gap between the spiral arms, where overlapping CO and Hα emission appears common, and the center. CO emission remains visible in this gap, while Hα emission appears to be largely absent. In NGC 3627 particular, the phenomenon is harder to identify because of the brightness of star-forming complexes at the bar ends (e.g., see Beuther et al. 2017). A similar depression in star formation has been identified along the spiral arms in NGC 5194 and attributed to streaming motions along the spiral arms (not a stellar bar) by Meidt et al. (2013).

In theoretical calculations, the high shear and/or diverging streamlines (caused by changing orbits) present at the location of the gas lanes along the stellar bar either prevent clouds from forming or tears them apart before star formation can happen (e.g. Athanassoula 1992; Regan et al. 1997). Observationally, this "star formation desert" (along the stellar bar) is not evident in all barred galaxies (see e.g. Sheth et al. 2000; James & Percival 2018). This suggests that the exact bar properties and/or the time evolution of bars may also be important to the suppression of star formation.

Overall, our data provide support for the idea that star formation in molecular gas is inhibited along many stellar bars. Despite the presence of bright CO emission, HII regions appear less common in these regions.

Spiral arms: For several galaxies we find a pronounced spatial offset between CO and Hα emission along spiral arms. In these cases, we observe a general pattern where *CO only* sightlines are more prominent on the concave side, while *overlap* sightlines are found along the convex side of a spiral arm, with *Hα only* sightlines sitting outside the *overlap* regions away from the *CO only* regions.

Figure 2 shows impressive examples of this phenomenon in the grand design spiral galaxies NGC 0628 (particular at smaller galactocentric radii; see also Fig. 1 in Kreckel et al. 2018) and NGC 5194 (e.g. Schinnerer et al. 2013, 2017). The spiral arms emanating from the stellar bars in NGC 4321 and NGC 4535 also exhibit offsets along significant arm segments. This suggests that a similar mechanism causes this offset in grand-design spirals and spiral arms dynamically linked to stellar bars. Assuming the spiral arms are trailing, the Hα offsets occur on the downstream side consistent with expectations for a rotating spiral density wave (inside co-rotation) (for a sketch see, e.g., Fig. 1 of Pour-Imani et al. 2016).

Trends with global properties: We compared the overlap fraction and amount of apparently quiescent CO emission to the integrated properties of the host galaxy, including stellar mass (M_{star}), star formation rate (SFR)

and specific SFR (sSFR≡SFR/M_{star}). While our sample of 8 galaxies represents a significant improvement compared to previous work, a much larger sample will be required to measure quantitative relationships. Still, some trends are already evident from these first results.

First, targets that have a large fraction of *CO only* sightlines at 140 pc resolution are all more massive than $\log(M_\star[M_\odot]) = 10.2$, tend to have higher SFRs ($SFR[M_\odot yr^{-1}] > 2$), and also tend to lie above the average stellar mass–SFR relation. Such galaxies tend to be rich in molecular gas compared to lower mass and more quiescent galaxies. This result suggests that, at least at any given moment, a large fraction of the gas in such galaxies may not be immediately associated with high mass star formation. We do caution that our present sample is heavily biased towards such objects.

By contrast, *Hα only* sightlines are most prominent in the two lowest mass and lowest SFR galaxies which also have the latest (NGC 5068) and earliest Hubble type (NGC 3351) of the sample. Though we do not include M33 in the analysis, this would appear to be consistent with the widespread Hα and confined CO emission visible in that galaxy (e.g., see Schruba et al. 2010; Druard et al. 2014; Corbelli et al. 2017). Here, sensitivity, conversion factor effects, and the choice of thresholds will play an important role, because these are also among our most quiescent targets.

The one galaxy where *overlap* sightlines dominate (NGC 3627) exhibits on average low SFR and sSFR values and is also part of a group currently undergoing a large-scale interaction.

No trend with the presence or absence of a (large-scale) stellar bar is evident. Similarly, we find no clear trend with the presence or absence of an AGN (all galaxies with $\log(M_\star(M_\odot) \gtrsim 10.4$, i.e. 5/8 galaxies, show evidence for an AGN). This is not surprising given the small sample size, the relatively low number of sightlines directly associated with the galaxy center or bar, and the temporal evolution expected for both phenomena.

Does feedback or galactic dynamics drive the CO morphology? In a series of recent papers, Semenov et al. (2017, 2018) put forward a star formation model based on high resolution simulations of gas and star formation in galaxy disks. Semenov et al. (2018) distinguish two distinct regimes, which may relate to the morphology of CO and Hα emission seen in our observations. In the "self-regulation" regime, the lifetime of gas in the star-forming state is limited by consumption via star formation and feedback. A stochastic, patchy appearance might be expected, with the CO emission shaped by stellar feedback. By contrast, in the "dynamics-regulation" regime, the lifetime of the star-forming gas is limited by dynamical processes. In this case, they expect the star formation to reflect the underlying distribution of the cold gas rather than being shaped by star formation and/or associated feedback.

In our observations, both the star-forming and quiescent molecular gas trace distinct bars, rings, and arms in most galaxies. In other words, it appears that the star formation traces the underlying molecular gas distribution, which in turn traces the underlying potential (see Fig. 4). The patchy stochastic appearance that we might expect for morphology dominated by self-regulation is most prominent in the outer disk of NGC 3351 and the low mass galaxy NGC 5068. This qualitative comparison, as well as the discussion above, demonstrates that the different dynamical environments and host galaxy properties do lead to varying conditions for star formation and that a simple assumption of self-regulation by stellar feedback that results in stochastic, isolated regions is probably too simplistic for many galaxies.

5.4. *Distributions by luminosity vs. distributions by area and role of galaxy centers*

For three of our targets, bright CO emission from the center (see Fig. 1; NGC 3351, NGC 4321, and NGC 4535) makes a large fractional contribution to the total CO luminosity (e.g., see flux-weighted histograms in Figure 1 of Sun et al. 2018). When we consider the distribution of flux, these bright centers exert a large influence on the fractions of emission associated with *CO only*, *Hα only*, and *overlap* regions (see Fig. 9 and Tab. 4). Because they cover relatively little area, the centers have a weaker effect on the distributions of covering fraction.

Excluding the centers leads to a slightly better agreement between a flux-weighted approach and a sightline-based approach. There are still differences between the two approaches, however. In general, the fraction of luminosity associated with *overlapping* CO and Hα is larger than the fraction of *overlapping* sightlines. This implies that the intensity of CO emission is higher in regions that also show Hα emission and, similarly, that the brighter Hα emission is associated with regions of higher CO emission.

Brighter CO emission in regions with Hα emission could be expected if star formation increases the temperature and excitation of the CO gas. This appears to be the case in a subset of our targets (T. Saito; priv. comm.). It may also reflect that the molecular gas structure differs between actively star-forming regions and quiescent regions. This also appears to be the case, with higher surface density gas being associated with active regions.

5.5. *Impact of methodology and next steps*

We adopt relatively simple methods to identify pixels tracing CO emission and likely HII regions that could bias our results. It also highlights natural next steps as we apply the method to a larger sample of galaxies.

Our fixed CO threshold leads to variable completeness across our sample (see Sun et al. 2018). Specifically, using our fixed threshold, we recover a lower fraction of the total CO emission in low mass galaxies and outer disks compared to massive spiral galaxies. Hughes et al. (2013) showed that molecular clouds in such systems have lower molecular gas surface densities (see also Sun et al. 2018; Schruba et al. 2019). This appears strongest in NGC 5068 and the outer part of NGC 3351, but may be present at large radii in most of our sample.

A bias against recovering all of the CO emission present affects the inferred f_{scale}, driving the apparent cycling time to artificially low values. Future work will need to address that the CO emission in some regions of our sample is faint compared to our sensitivity. This can be achieved by using statistical methods that account for the effects of noise and by informing the measurements using the known total CO flux from each region of the galaxy.

Local variations of the CO-to-H_2 conversion factor, α_{CO}, could also impact our analysis. In this case, our estimates for CO-emitting fractions "by flux" would no longer straightforwardly correspond to a mass fraction of the molecular gas reservoir. Moreover, the meaning of our adopted threshold would change across the galaxy. Previous work does not suggest enormous α_{CO} variations across this specific sample. Sandstrom et al. (2013) derived α_{CO} at ∼kpc resolution for five galaxies in our sample (NGC 0628, NGC 3351, NGC 3627, NGC 4254, NGC 4321) and saw no significant variations across the disks or with radius (excluding some central depression which cover only a small area in our analysis). Similarly, Leroy et al. (2017a) found a basically constant α_{CO} across the PAWS area in NGC 5194. Nonetheless, in a preliminary comparison, we do find some modest differences between molecular cloud properties and CO excitation in the *CO only* regions and *overlap* regions.

Likewise, our identification method for HII regions in narrowband Hα maps has an impact on our results. If we insufficiently subtract the DIG, we expect to find an artifical increase of *Hα only* sightlines at small scales. This, in turn, will drive f_{scale} to artificially low values. Though we inspected our images and verified our algorithm works to first order, adopting a single simple algorithm to analyze galaxy centers, spiral arms, and low density flocculent galaxies will likely yield significant biases. Compounding this situation, the Hα line emission is significantly affected by extinction, and both flux-based approaches and the interpretation of thresholds depend on local, robust extinction corrections.

More sophisticated morphological separation methods (e.g., newer versions of HIIPHOT; Thilker et al. 2000) offer some prospect to improve the situation. The main hope for improvement here comes from the use of optical integral field spectroscopy (IFS). IFS allows for simultaneous correction for internal extinction and improved tools for distinguishing the Hα emission from DIG and shocks or X-ray Dominated Regions (XDRs) associated with AGN. VLT/MUSE IFS data are currently being obtained for ∼ 19 PHANGS targets, which have the prospect to then act as a training set for improved morphological and multi-wavelength methods for HII region identification and extinction corrections. Initial tests on the MUSE data for four galaxies yield HII region masks that are more restricted than those constructed in § 2.2.5. This suggests that our HII region identification scheme may bias us to slightly low f_{scale} and thus shorter CO-emitting region lifetimes.

Despite these caveats, we emphasize that most of our analysis focuses on the presence or absence of CO or Hα emission, not their exact translation into physical quantities. We made this choice exactly to minimize the bias due to uncertain conversions between CO and H_2 or Hα and a local star formation rate.

6. SUMMARY AND CONCLUSIONS

We compare high angular resolution observations of CO line emission to narrowband Hα imaging in eight nearby star-forming galaxies. We use PHANGS-ALMA CO (2-1) imaging for seven targets and a PdBI CO (1-0) map for one target. The Hα data come from a mixture of new and literature sources. Together, the data allow us to compare the distributions of molecular gas and star formation at a common spatial scale of 140 pc. This represents roughly an order of magnitude increase in sample size compared to previous high resolution comparisons of CO and Hα emission, which have mostly compared highly resolved CO and Hα in individual Local Group galaxies.

We use these data to study the spatial relationship between the cold molecular gas reservoir and H II regions, which serve as signposts of recent high-mass star formation. We adopt a simple, reproducible methodology that quantifies overlap between the tracers, in both area and flux, as a function of scale. We classify each line of sight at each scale according to its contents: it either contains *only CO*, *only Hα*, or *overlapping* CO and Hα emission. We measure the fraction of area in each cat-

egory as a function of the resolution of the data. Our main findings are:

1. *CO only* emission (corresponding to H_2 surface densities of $\gtrsim 12.6\,M_\odot pc^{-2}$) without associated H$\alpha$ emission (above SFR surface densities of 0.0014 and $0.0036\,M_\odot\,yr^{-1}\,kpc^{-2}$ depending on the galaxy target) is very common in our sample at 140 pc resolution. Our targets show a median of $\sim$ 40% of detected sightlines in this category, though this numerical value is specific to our adopted thresholds for CO and Hα emission. Taken at face value, this implies a large amount of molecular gas without associated recent high-mass star formation. This gas may be in the process of collapsing, may be dynamically unsuited to form stars, or may already be forming low-mass stars.

2. Lines of sight where CO and Hα *overlap* represent the next most common category, also accounting for median $\sim$ 40% of the sightlines at 140 pc resolution. That is, H II regions typically coincide with molecular gas at this resolution. Our lowest mass target and our earliest Hubble type system represent notable exceptions to this statement. In those targets, HII region sightlines are the most common type of sightline. We note some concerns related to the impact of completeness, adopted thresholds, and conversion factor on our results for these targets.

3. The balance between *CO only*, *Hα only*, and *overlapping* lines of sight is a strong function of spatial scale. As we degrade the resolution of our maps, the fraction of *CO only* emission – tracing apparently quiescent molecular gas – decreases, while a steadily increasing fraction of the CO emission becomes associated with *overlapping* sightlines. By 1 kpc resolution, $\sim$ 75% of all sightlines, on average, show overlapping Hα and CO emission. At resolutions coarser than $\sim$ 1 kpc, the main morphological features of our sample galaxies are indistinct. Little information about the relative distributions of CO and Hα emission or their relation to galactic morphology remains at these coarse resolutions. This behavior is consistent with literature results that report a decrease in the scatter of the scaling relations when going from small to large scales.

4. At 140 pc resolution, the spatial distributions of both CO emission and H II regions follow galactic structures such as rings, spiral arms and bars. CO emission appears to faithfully trace these "backbones" of the underlying galactic potential. This highlights the role of these stellar structures in organizing the molecular gas reservoir and star formation. Hα emission follows these structures as well, but in a more spotty fashion. Compared to the CO emission, Hα emission appears more localized. This patchy appearance of the H II regions partially reflects our processing of the Hα maps to remove the DIG contribution, and the sensitivity of our Hα data.

5. Taking the simplest statistical approach, our galaxy-averaged measurements of the fractions of sightlines with CO, Hα emission or both at 140 pc resolution imply that, on average, molecular gas cycles through a non-star-forming state to a star-forming state and then is dispersed on a median timescale that is 1.4$\times$ longer than the visibility time for Hα emission (i.e., $\sim$ 10$-$15 Myr). Considering that the physical resolution of our data does not yet attain the characteristic size of molecular clouds and H II regions in the Milky Way, we expect that this timescale represents a lower limit.

6. Hα emission appears offset from CO in strong spiral arms, in the sense that the Hα emission tends to lie along the convex side of the spiral arm compared to the CO emission. Hα emission is weak or absent along some stellar bars, while sightlines along the (often linear) gas lanes along strong bars frequently show *CO only* emission. Both these results reflect the influence of dynamical features on the molecular gas distribution and star formation activity in our galaxies.

7. We find some trend between the *overlap* fraction (computed at 140 pc resolution) and the fraction of recovered total CO flux in the maps. Further we see some evidence for trends relating stellar mass, SFR, and sSFR to the overall balance between *CO only*, *Hα only*, and *overlap* fractions. The sense of the trends is that massive, high-SFR, high-sSFR galaxies tend to show high *CO only* fractions. Confirming these trends will require analysis of a significantly larger and more diverse sample.

The methodology presented in this paper can be easily applied to much larger samples, including the full PHANGS-ALMA and paired Hα survey now underway. This larger sample should allow us to identify potential trends with global galaxy parameters more robustly. In

particular, more sensitive maps of dwarf spirals and the outer parts of galaxies should help illuminate the nature of systems like NGC 5068 and NGC 3351 which showed distinctly different trends from the remaining sample. Other follow-up studies (utilizing a larger sample) include the detailed investigation of how physical properties of the CO-traced molecular gas vary between star-forming and non-star-forming regions, and how galactic dynamics drives the suppression of star formation.

A straightforward future extension of the methodology is the implementation of a more generalized form utilizing the information from the cross-distribution of the CO and Hα emission (via calculating cross cumulative distribution functions, xCDFs) without the need to establish flux thresholds, and compare this information from xCDFs with those from traditional CDFs. This kind of analysis offers a robust, rich way to characterize the joint distributions of CO and Hα emission in galaxies, yielding measurements ideally suited for comparison with simulations. As well as trends with galactocentric radius, comparing the statistics of both traditional and 'cross' distributions among different galactic environments should provide further insight on how local conditions influence star formation and feedback.

This work was carried out as part of the PHANGS collaboration. We thank the anonymous referee for constructive feedback that helped improve the manuscript. We thank B. Venemans for help with the absolute astrometric calibration of the Hα maps used for analysis. ES, CF, and TS acknowledge funding from the European Research Council (ERC) under the European Unions Horizon 2020 research and innovation programme (grant agreement No. 694343). AH acknowledges support by the Programme National Cosmology et Galaxies (PNCG) of CNRS/INSU with INP and IN2P3, co-funded by CEA and CNES, and by the Programme National Physique et Chimie du Milieu Interstellaire (PCMI) of CNRS/INSU with INC/INP co-funded by CEA and CNES. The work of AKL is partially supported by the National Science Foundation under Grants No. 1615105, 1615109,and 1653300. AKL also acknowledges partial support from NASA ADAP grants NNX16AF48G and NNX17AF39G. BG gratefully acknowledges the support of the Australian Research Council as the recipient of a Future Fellowship (FT140101202). KK gratefully acknowledges support from grant KR 4598/1-2 from the DFG Priority Program 1573. FB acknowledges funding from the European Research Council (ERC) under the European Unions Horizon 2020 research and innovation programme (grant agreement No. 726384). SG acknowledges support from the Deutsche Forschungsgemeinschaft via the Collaborative Research Centre (SFB 881) "The Milky Way System" (subprojects B1, B2, and B8) and from the Heidelberg cluster of excellence EXC 2181 "STRUCTURES: A unifying approach to emergent phenomena in the physical world, mathematics, and complex data" funded by the German Excellence Strategy. JMDK and MC acknowledge funding from the German Research Foundation (DFG) in the form of an Emmy Noether Research Group (grant number KR4801/1-1), and the DFG Sachbeihilfe (grant number KR4801/2-1). JMDK acknowledges funding from the European Research Council (ERC) under the European Unions Horizon 2020 research and innovation programme via the ERC Starting Grant MUSTANG (grant agreement number 714907). JP acknowledges support from the Programme National Physique et Chimie du Milieu Interstellaire (PCMI) of CNRS/INSU with INC/INP co-funded by CEA and CNES. ER acknowledges the support of the Natural Sciences and Engineering Research Council of Canada (NSERC), funding reference number RGPIN-2017-03987. The work of JS amd DU is partially supported by the National Science Foundation under Grants No. 1615105, 1615109, and 1653300. This paper makes use of the following ALMA data: ADS/JAO.ALMA #2012.1.00650.S, ADS/JAO.ALMA #2015.1.00925.S, ADS/JAO.ALMA #2015.1.00956.S. ALMA is a partnership of ESO (representing its member states), NSF (USA) and NINS (Japan), together with NRC (Canada), NSC and ASIAA (Taiwan), and KASI (Republic of Korea), in cooperation with the Republic of Chile. The Joint ALMA Observatory is operated by ESO, AUI/NRAO and NAOJ. The National Radio Astronomy Observatory is a facility of the National Science Foundation operated under cooperative agreement by Associated Universities, Inc. This paper makes use of the PdBI Arcsecond Whirlpool Survey (Schinnerer et al. 2013; Pety et al. 2013). The IRAM 30m telescope and PdBI are run by IRAM, which is supported by INSU/CNRS (France), MPG (Germany) and IGN (Spain). This work has made use of data from the European Space Agency (ESA) mission *Gaia* (https://www.cosmos.esa.int/gaia), processed by the *Gaia* Data Processing and Analysis Consortium (DPAC, https://www.cosmos.esa.int/web/gaia/dpac/consortium). Funding for the DPAC has been provided by national institutions, in particular the institutions participating in the *Gaia* Multilateral Agreement.

Facilities: ALMA, IRAM (PdBI and 30m), MPG 2.2m (WFI)

APPENDIX

A. EXCLUDING THE CENTRAL REGIONS OF GALAXIES

About half the galaxies in our sample show a non-neglible difference in the fractions of quiescent and star-forming molecular gas when these fractions are defined by sightline or by flux (see § 4.1). To test whether CO-bright galaxy centers are responsible for this difference, we repeat our analysis presented in that section, excluding the central region from our measurements. For simplicity, we adopt the central region definition used by Sun et al. (2018), i.e. we define the center as the region within 1 kpc of the galaxy reference position (see Table 1). We follow Sun et al. (2018) who adopted a larger radius of 1.5 kpc so that the visually distinct inner disk is entirely inside the central region of NGC 3351. The resulting resulting fractions are listed in Tab. 6 and Tab. 7 and compared in Fig. 9. As can be seen

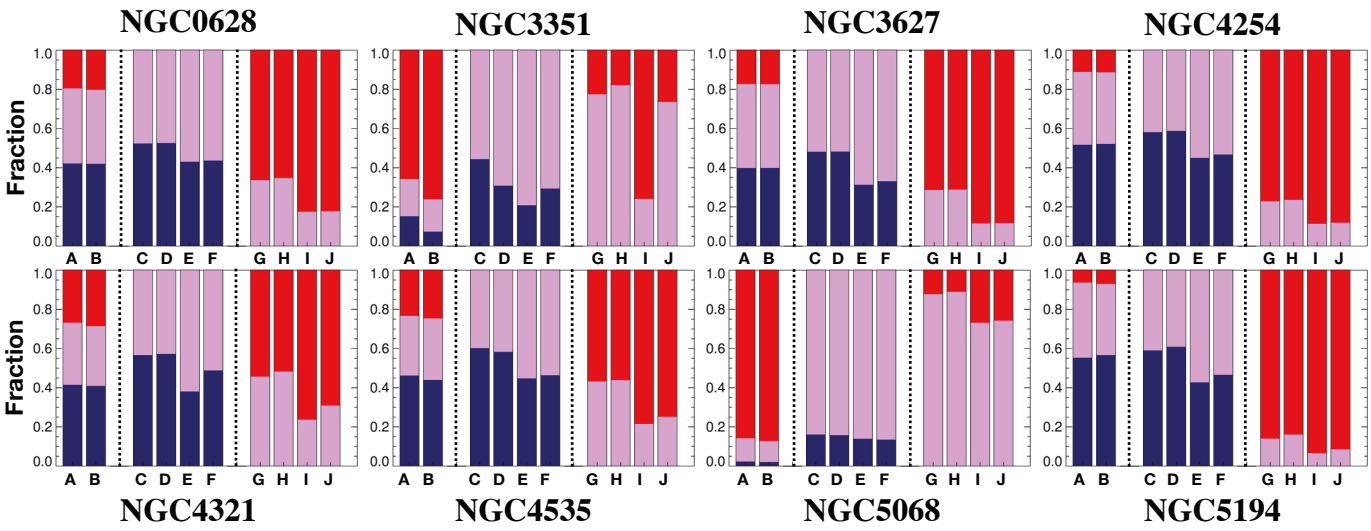

Figure 9. Bar graphs summarizing the impact of different assumptions (sightlines vs. flux; full FoV vs. disk only) for the different fractions of pixels in our sample galaxies. The color coding is dark blue – *CO only*, red – *Hα only*, lavender – *overlap*. The bar graphs for each individual galaxy show the following (labels as indicated on the x-axis): relative distribution of *CO only*, *Hα only* and *overlap* sightlines for our FoV (**A**, analoguous to Fig. 3) and disk only (**B**); relative distribution of sightlines tracing CO emission for our FoV (**C**) and disk only (**D**) vs. distribution of CO flux (**E** – our FoV, **F** – disk only); and relative distribution of sightlines tracing Hα emission for our FoV (**G**) and disk only (**H**) vs. distribution of Hα flux (**I** – our FoV, **J** – disk only).

REFERENCES

Athanassoula, E. 1992, MNRAS, 259, 345

Azimlu, M., Marciniak, R., & Barmby, P. 2011, AJ, 142, 139

Battersby, C., Bally, J., & Svoboda, B. 2017, ApJ, 835, 263

Beuther, H., Meidt, S., Schinnerer, E., Paladino, R., & Leroy, A. 2017, A&A, 597, A85

Bigiel, F., Leroy, A., Walter, F., et al. 2008, AJ, 136, 2846

Bigiel, F., Leroy, A. K., Walter, F., et al. 2011, ApJL, 730, L13

Blanc, G. A., Heiderman, A., Gebhardt, K., Evans, N. J., II, & Adams, J. 2009, ApJ, 704, 842

Blanc, G. A., Weinzirl, T., Song, M., et al. 2013, AJ, 145, 138

Bohlin, R. C., Savage, B. D., & Drake, J. F. 1978, ApJ, 224, 132

Bolatto, A. D., Wolfire, M., & Leroy, A. K. 2013, ARA&A, 51, 207

Bolatto, A. D., Wong, T., Utomo, D., et al. 2017, ApJ, 846, 159

Bradley, T. R., Knapen, J. H., Beckman, J. E., & Folkes, S. L. 2006, A&A, 459, L13

Table 6. Line of Sight Fractions between Tracers at 140 pc Scale for Disks Only.

Name	CO only	Hα only	overlap
	(%)	(%)	(%)
NGC0628	42	20	38
NGC3351	7	76	17
NGC3627	40	17	43
NGC4254	52	11	37
NGC4321	41	29	31
NGC4535	44	25	31
NGC5068	2	87	11
NGC5194	57	7	36
Median	42	25	36
Mean	36	34	30

NOTE—Fraction of sightlines with CO emission only, Hα emission only, and both CO and Hα emission *for disks only*, i.e. excluding emission arising inside the central region. This table is analogous to Tab. 3 in the main text. Note that the medians are not re-normalized, thus the sum will not add up to 100%.

Table 7. Line of Sight and Flux Fractions per Tracer at 140 pc Scale.

	By Number				By Flux			
	CO Sightlines		Hα Sightlines		CO Flux		Hα Flux	
Name	CO only	CO overlap	Hα only	Hα overlap	CO only	CO overlap	Hα only	Hα overlap
	(%)	(%)	(%)	(%)	(%)	(%)	(%)	(%)
NGC 0628	51	49	36	64	42	58	20	80
NGC 3351	35	65	74	26	33	67	61	39
NGC 3627	38	62	34	66	23	77	14	86
NGC 4254	58	42	18	82	43	57	10	90
NGC 4321	65	35	40	60	54	46	25	75
NGC 4535	63	37	40	60	50	50	24	76
NGC 5068	20	80	88	12	17	83	68	32
NGC 5194	60	40	17	83	46	54	9	91
Median	55	45	36	64	42	58	20	80
Mean	49	51	41	59	39	61	27	73

NOTE—Fraction of sightlines with *CO only* emission, *Hα only* emission, and both CO and Hα *overlapping* emission *for disks only*, i.e. excluding emission arising from within the central region. This table is analogous to Tab. 4 in the main text. Note that the medians are not re-normalized, thus the sum will not add up to 100%.

Caldú-Primo, A., Schruba, A., Walter, F., et al. 2015, AJ, 149, 76

Chandar, R., Whitmore, B. C., Calzetti, D., et al. 2011, ApJ, 727, 88

Chevance, M., et al. 2019, MNRAS, subm.

Clark, P. C., & Glover, S. C. O. 2015, MNRAS, 452, 2057

Colombo, D., Hughes, A., Schinnerer, E., et al. 2014, ApJ, 784, 3

Comerón, S., Knapen, J. H., Beckman, J. E., et al. 2010, MNRAS, 402, 2462

Corbelli, E., Braine, J., Bandiera, R., et al. 2017, A&A, 601, A146

Davis, T. A., Young, L. M., Crocker, A. F., et al. 2014, MNRAS, 444, 3427

Dobbs, C. L., & Pringle, J. E. 2013, MNRAS, 432, 653

Dobbs, C. L., Pringle, J. E., & Duarte-Cabral, A. 2015, MNRAS, 446, 3608
Druard, C., Braine, J., Schuster, K. F., et al. 2014, A&A, 567, A118
Dunham, M. M., Stutz, A. M., Allen, L. E., et al. 2014, Protostars and Planets VI, 195
Egusa, F., Mentuch Cooper, E., Koda, J., & Baba, J. 2017, MNRAS, 465, 460
Elmegreen, B. G. 2000, ApJ, 530, 277
Evans, N. J., Dunham, M. M., Jørgensen, J. K., et al. 2009, ApJS, 181, 321
Faesi, C. M., Lada, C. J., Forbrich, J., et al. 2014, ApJ, 789, 1, 81
Feldmann, R., Gnedin, N. Y., & Kravtsov, A. V. 2011, ApJ, 732, 115
Fukui, Y., & Kawamura, A. 2010, ARA&A, 48, 547
Gaia Collaboration, Brown, A. G. A., Vallenari, A., et al. 2016, A&A, 595, A2
Gaia Collaboration, Brown, A. G. A., Vallenari, A., et al. 2018, A&A, 616, A1
Gratier, P., Braine, J., Rodriguez-Fernandez, N. J., et al. 2012, A&A, 542, A108
Haffner, L. M., Dettmar, R.-J., Beckman, J. E., et al. 2009, Reviews of Modern Physics, 81, 969
Haydon, D. T., Kruijssen, J. M. D., Hygate, A. P. S., et al. 2018, arXiv e-prints, arXiv:1810.10897
Heiderman, A., Evans, N. J., Allen, L. E., et al. 2010, ApJ, 723, 1019
Heyer, M., & Dame, T. M. 2015, ARA&A, 53, 583
Heyer, M., Krawczyk, C., Duval, J., et al. 2009, ApJ, 699, 1092
Hirota, A., Egusa, F., Baba, J., et al. 2018, PASJ, 70, 73
Hughes, A., Meidt, S. E., Colombo, D., et al. 2013, ApJ, 779, 46
James, P. A., & Percival, S. M. 2018, MNRAS, 474, 3101
Kaplan, K. F., Jogee, S., Kewley, L., et al. 2016, MNRAS, 462, 1642
Kawamura, A., Mizuno, Y., Minamidani, T., et al. 2009, ApJS, 184, 1
Kennicutt, R. C., Jr. 1998, ApJ, 498, 541
Kennicutt, R. C., Jr. 1998, ARA&A, 36, 189
Kennicutt, R. C., Jr., Armus, L., Bendo, G., et al. 2003, PASP, 115, 928
Kennicutt, R. C., Calzetti, D., Aniano, G., et al. 2011, PASP, 123, 1347
Kennicutt, R. C., & Evans, N. J. 2012, ARA&A, 50, 531
Knapen, J. H., Stedman, S., Bramich, D. M., Folkes, S. L., & Bradley, T. R. 2004, A&A, 426, 1135
Kreckel, K., Blanc, G. A., Schinnerer, E., et al. 2016, ApJ, 827, 103
Kreckel, K., Groves, B., Schinnerer, E., et al. 2013, ApJ, 771, 62
Kreckel, K., Faesi, C., Kruijssen, J. M. D., et al. 2018, ApJL, 863, L21
Kruijssen, J. M. D., & Longmore, S. N. 2014, MNRAS, 439, 3239
Kruijssen, J. M. D., Pfeffer, J. L., Reina-Campos, M., et al. 2019, MNRAS, 486, 3180
Kruijssen, J. M. D., Schruba, A., Hygate, A. P. S., et al. 2018, MNRAS, 479, 1866
Krumholz, M. R., & McKee, C. F. 2005, ApJ, 630,
Lee, E. J., Miville-Deschênes, M.-A., & Murray, N. W. 2016, ApJ, 833, 229
Leroy, A. K., Bigiel, F., de Blok, W. J. G., et al. 2012, AJ, 144, 3
Leroy, A. K., Hughes, A., Schruba, A., et al. 2016, ApJ, 831, 16
Leroy, A. K., Sandstrom, K. M., Lang, D., et al. 2019, ApJS, 244, 24
Leroy, A. K., Schinnerer, E., Hughes, A., et al. 2017, ApJ, 846, 71
Leroy, A. K., Walter, F., Brinks, E., et al. 2008, AJ, 136, 2782
Leroy, A. K., Walter, F., Sandstrom, K., et al. 2013, AJ, 146, 19
Leroy, A. K., et al. 2019, XXX, in prep.
Levy, R. C., Bolatto, A. D., Sánchez, S. F., et al. 2019, ApJ, 882, 84
Liu, G., Koda, J., Calzetti, D., Fukuhara, M., & Momose, R. 2011, ApJ, 735, 63
Liu, G., Calzetti, D., Kennicutt, R. C., Jr., et al. 2013, ApJ, 772, 27
Meidt, S. E., et al. 2019, ApJ, subm.
Meidt, S. E., Hughes, A., Dobbs, C. L., et al. 2015, ApJ, 806, 72
Meidt, S. E., Schinnerer, E., García-Burillo, S., et al. 2013, ApJ, 779, 45
Meurer, G. R., Hanish, D. J., Ferguson, H. C., et al. 2006, ApJS, 165, 307
Momose, R., Koda, J., Kennicutt, R. C., Jr., et al. 2013, ApJL, 772, L13
Monet, D. 1998, USNO-A2.0, by Monet, David. [Flagstaff, AZ] : U.S. Naval Observatory, c1998. . United States Naval Observatory.,
Oey, M. S., Parker, J. S., Mikles, V. J., & Zhang, X. 2003, AJ, 126, 2317
Oey, M. S., Meurer, G. R., Yelda, S., et al. 2007, ApJ, 661, 801
Onodera, S., Kuno, N., Tosaki, T., et al. 2010, ApJL, 722, L127

Ostriker, E. C., McKee, C. F., & Leroy, A. K. 2010, ApJ, 721, 975
Pety, J., Schinnerer, E., Leroy, A. K., et al. 2013, ApJ, 779,
Pour-Imani, H., Kennefick, D., Kennefick, J., et al. 2016, ApJL, 827, L2
Querejeta, M., Schinnerer, E., Schruba, A., et al. 2019, A&A, 625, A19
Razza, A., et al. 2019, in prep.
Regan, M. W., Vogel, S. N., & Teuben, P. J. 1997, ApJL, 482, L143
Renaud, F., Famaey, B., & Kroupa, P. 2016, MNRAS, 463, 3637
Roman-Duval, J., Heyer, M., Brunt, C. M., et al. 2016, ApJ, 818, 144
Rossa, J., & Dettmar, R.-J. 2003, A&A, 406, 505
Rousseau-Nepton, L., Robert, C., Martin, R. P., et al. 2018, MNRAS, 477, 4152
Saintonge, A., Kauffmann, G., Wang, J., et al. 2011, MNRAS, 415, 61
Saintonge, A., Catinella, B., Tacconi, L. J., et al. 2017, ApJS, 233, 22
Sanders, D. B., Scoville, N. Z., & Solomon, P. M. 1985, ApJ, 289, 373
Sandstrom, K. M., Leroy, A. K., Walter, F., et al. 2013, ApJ, 777, 5
Schinnerer, E., Meidt, S. E., Pety, J., et al. 2013, ApJ, 779, 42
Schinnerer, E., Meidt, S. E., Colombo, D., et al. 2017, ApJ, 836, 62
Schlafly, E. F., & Finkbeiner, D. P. 2011, ApJ, 737, 103
Schruba, A., Kruijssen, J. M. D., & Leroy, A. K. 2019, ApJ, 883, 2
Schruba, A., Leroy, A. K., Walter, F., Sandstrom, K., & Rosolowsky, E. 2010, ApJ, 722, 1699
Schruba, A., Leroy, A. K., Walter, F., et al. 2011, AJ, 142, 37
Scoville, N. Z., Polletta, M., Ewald, S., et al. 2001, AJ, 122, 3017
Semenov, V. A., Kravtsov, A. V., & Gnedin, N. Y. 2017, ApJ, 845, 133
Semenov, V. A., Kravtsov, A. V., & Gnedin, N. Y. 2018, ApJ, 861, 4
Sharma, S., Corbelli, E., Giovanardi, C., Hunt, L. K., & Palla, F. 2011, A&A, 534, A96
Sheth, K., Regan, M. W., Vogel, S. N., et al. 2000, ApJ, 532, 221
Sun, J., Leroy, A. K., Schruba, A., et al. 2018, ApJ, 860, 172
Thilker, D. A., Braun, R., & Walterbos, R. A. M. 2000, AJ, 120, 3070
Thilker, D. A., Walterbos, R. A. M., Braun, R., & Hoopes, C. G. 2002, AJ, 124, 3118
Tomičić, N., Kreckel, K., Groves, B., et al. 2017, ApJ, 844, 155
Weilbacher, P. M., Monreal-Ibero, A., Verhamme, A., et al. 2018, A&A, 611, A95
Whitaker, K. E., Pope, A., Cybulski, R., et al. 2017, ApJ, 850, 208
Whitmore, B. C., Chandar, R., Kim, H., et al. 2011, ApJ, 729, 78
Wong, T., & Blitz, L. 2002, ApJ, 569, 157
Utomo, D., Sun, J., Leroy, A. K., et al. 2018, ApJL, 861, L18
Young, J. S., Xie, S., Tacconi, L., et al. 1995, ApJS, 98, 219